CrystEngComm

Accepted Manuscript

ROYAL SOCIETY OF CHEMISTRY

www.rsc.org/crystengcomm

Journal Name

RSCPublishing

ARTICLE

Influence of sol counter-ions on the anatase-to-rutile phase transformation and microstructure of nanocrystalline TiO_2

Cite this: DOI: 10.1039/x0xx00000x

Received 00th January 2012,
Accepted 00th January 2012

DOI: 10.1039/x0xx00000x

www.rsc.org/

D.M. Tobaldi,[a] R.C. Pullar,[a] A.F. Gualtieri,[b] A. Belen Jorge,[c] R. Binions,[d] M.P.Seabra[a] and J.A. Labrincha[a]

Amongst nanomaterials, metal oxides are playing an increasingly dominant role, with titanium dioxide (titania, TiO_2) being widely used for various applications, such as light-to-energy conversion and storage, and photocatalysis. In this work, TiO_2 has been synthesised *via* an aqueous sol-gel method, using three different mineral acids (HNO_3, HCl and HBr) to peptise the sol, and hence provide counter-ions. Dried sols were thermally treated at three different temperatures (450, 600 and 800 °C), using three different dwell times (2, 4, and 8 h). Advanced X-ray methods were used to monitor the effect that the counter-ions had on the anatase-to-rutile phase transformation (ART). Quantitative phase analysis (QPA) using the Rietveld method was applied to assess the true amount of crystalline phases in the systems, and the amount of amorphous phase. Furthermore, the average crystalline domain diameter was also investigated, using whole powder pattern modelling (WPPM). With those advanced XRPD data (actual crystalline phase weight fraction in the samples, and their average domain diameter and size distribution), it was possible to carry-out a semi-quantitative study of the ART transformation kinetics. At a low temperature of 75 °C, the Cl^- counter-ion was the most favourable to obtain anatase as the major crystalline phase, delaying the onset of the ART. Conversely, the Br^- ions, maintained more anatase at 450 °C, with a lower ART rate. In general, halides were more effective in delaying the ART than NO_3^-counterions. Moreover, we observed an inverse linear relationship between the lattice volume expansion of rutile and the increase of its crystalline domain size at 450 and 600 °C isotherms. As the domain sizes increased with temperature this effect reversed and became a direct linear dependence, at the 800 °C isotherm, suggesting a critical size limit for this effect <90 nm.

Introduction

The development of nanotechnologies is currently one of the hot topics in Materials science. This is because nanomaterials possess unique physiochemical, catalytic, surface and magnetic properties, providing solutions to problems that cannot be dealt with using conventional technologies. Because of their abundance and relatively low cost (compared to noble metals), metal oxides have become the most convenient materials in many catalytic applications, and are playing a dominant role in the era of nanotechnology.[1] Titanium dioxide (titania, TiO_2), deserves a special mention, as it is not only widely used as whitener or desiccant in cosmetics, packaged foods and household products,[2] but, due to its non-toxic nature, wide band-gap energy and stability in both acidic and alkaline media, it is also commonly used for light energy conversion and storage[3–5] and for photocatalytic applications.[6–8]

TiO_2 crystallises in a large number of polymorphs[9] − there are actually eleven described bulk / nano-crystalline TiO_2 phases, together with at least three non-crystalline TiO_2 phases[10] − although the best known ones are (in order of abundance) rutile, anatase and brookite.[11] Of these three polymorphs, the most thermodynamically stable phase is coarse-grained rutile,[12] having the lowest bulk free energy.[13,14] Upon heating, both brookite and anatase transform exothermally and irreversibly into rutile, in a metastable-to-stable transformation.[15–17] However, the thermodynamic stability of different titania phases is particle size dependent,[18]

and anatase is the polymorph having the lowest surface free energy at the nanoscale. Therefore, nano-TiO_2 usually consists of that phase, with a "critical size" of around 10-15 nm, above which rutile is supposed to become the main phase.[14]

The anatase-to-rutile phase transformation (ART) is of paramount importance at the nanoscale, as phase transformation and particle growth are influenced by the initial crystalline domain size. Hence, ART cannot be ignored in designing targeted nanostructures with attractive properties for numerous green energy applications.[19] Some authors report that the ART initiates at the junctions of particle-to-particle contact, and hence, the ART has been shown to be particle size dependent, as this determines the number of particle-particle contacts per unit volume.[20,21]

In this work, TiO_2 – taken as a model system, because of its increasing importance in many energy and environmental applications[22–27] – has been synthesised *via* an aqueous sol-gel method. Three different mineral acids were used to peptise the sol (HNO_3, HCl and HBr), providing the counter-ions. Small changes in the synthetic procedure can result in large changes in the physical and chemical properties of the products.[28–30] The dried sols were thermally treated at three different temperatures and three different dwell times, with the aim of monitoring the effect that the counter-ions had on the ART *via* X-ray methods such as Rietveld quantitative phase analysis (QPA). The average crystalline domain diameter (crystalline domains assumed to be spherical), and size distribution of crystallites in both the dried sols and thermally treated gels, was also investigated, using advanced whole powder pattern modelling (WPPM). With the obtained data (actual crystalline phase weight fraction in the samples, fraction of the amorphous phase, and their average domain diameter), it was possible to make a semi-quantitative comparison of the ART transformation kinetics between the systems used. This was an *ex-situ* preliminary study, intended to be followed and extended with a dedicated *in situ* XRPD study with both conventional and non-conventional (synchrotron) sources.

Furthermore, with the microstructural characterisation of TiO_2 we observed an inverse linear relationship between the lattice volume expansion of rutile and the increase of its crystalline domain size in samples thermally treated at 450 and 600 °C, which becomes a direct relationship at the higher thermal treatment temperature of 800 °C, for a rutile average crystalline domain diameter of approximately > 90 nm.

Experimental

Sample preparation

Aqueous titanium(IV)hydroxide sols were prepared following the procedure previously reported for nitrate-based sols,[31] but using three different mineral acids: HNO_3, HCl and HBr. This was achieved *via* the controlled hydrolysis and peptisation of titanium(IV)isopropoxide (Ti-*i*-pr, $Ti(OCH(CH_3)_2)_4$), using distilled water diluted in alcohol. The water/alcohol solution also contained the peptising acid. One part of Ti-*i*-pr (Aldrich, 97%) was added to four parts of isopropyl alcohol (IPA) to make a 20% vol Ti-*i*-pr solution. This Ti-*i*-pr solution was hydrolysed by the dropwise addition of an excess of water (5:1 water:Ti-*i*-pr), also as a 20% vol solution in IPA. The acid necessary to peptise the sol was also added to this water-IPA solution, in a molar ratio of Ti^{4+}:acid of 2.5:1. The acids used were concentrated HNO_3 (Aldrich, 65%), concentrated HCl (VWR AnalaR, 37%) and concentrated HBr (Aldrich, 48%). This water-IPA-acid solution was added dropwise to the Ti-*i*-pr solution at room temperature (RT) over about 40 min, whilst it was mechanically stirred at 800 RPM − 1 L beaker (100 mm in diameter), the radius of the mechanical stirrer was equal to 25 mm. The precipitated mixture was evaporated to a white jelly-like mass on a rotary evaporator at 60 ºC and 140 mPa, to remove the alcohol. Distilled water was added to restore the mixture to the original volume, the gelatinous mass was redispersed in a few min, and the aqueous mixture evaporated again, this time at 65 mPa and 60 ºC, to form to a partially dried, sticky gel. At this stage, when water was added again, the gel instantly dispersed to form a sol within 2 min, and the sol was diluted to a concentration of 1 M Ti^{4+}.

The as-synthesised gels were dried in an oven at 75 °C. Afterwards, the dried gels were heated in a muffle furnace at 450 °C, 600 °C and 800 °C, under a static air flow. The heating rate was 5 °C min^{-1}, with three different dwell times: 2, 4 and 8 hours at the selected temperature. Samples were named after the acid used, with a number standing for the maximum heating temperature reached and the dwell time (*i.e.* **HNO_3 450/2h** = HNO_3-based sol thermally treated at 450 °C / 2 h).

Sample characterisation

X-ray powder diffraction (XRPD) data for the quantitative phase analysis (QPA) were collected using a θ/θ diffractometer (PANalytical X'Pert Pro, NL) equipped with a fast RTMS detector (PANalytical PIXcel-1D) with Cu Kα radiation (40kV and 40 mA, 20-80 °2θ range, a virtual step scan of 0.0167 °2θ and virtual time per step of 50 s). 0.125° divergence and anti-scattering slits, 0.04 rad soller slits, and a 15 mm copper mask were mounted in the incident beam pathway. The pathway of the diffracted beam included a Ni filter, 0.04 rad soller slits and a 5 mm antiscatter blade. Full QPA (*i.e.* determination of both crystalline and amorphous content) was performed using the combined Rietveld and RIR methods, as previously reported by the authors:[9,32,33] 10 wt% corundum (NIST 676a) was added to the sample, and treated as an additional phase in the refinements. In this case, the refined weight fractions of each crystalline phase (W_{ic}) were rescaled with respect to the known weight fraction of the added standard (W_s) in order to obtain the real crystalline phase weight fraction (W_i):

$$W_i = \frac{1}{1-W_S}\left[\left(\frac{W_S}{W_{SC}}\right)W_{iC}\right] \quad (1)$$

where W_{sc} is the refined weight fraction of the internal standard. Knowing the weight fractions of all crystalline phases, the

amorphous content (W_a) was calculated using the following equation:

$$W_a = 1 - \sum_i W_i \quad (2)$$

For all XRPD measurements, the samples were sieved at 40 μm, gently ground in an agate mortar, and mounted in aluminium sample holders using the side-loading technique. The Rietveld data analysis was performed using the GSAS software suite with its graphical interface EXPGUI.[34,35] The starting atomic parameters for anatase, rutile and brookite, described by the space groups (SGs) $I4_1/amd$, $P4_2/mnm$, and $Pbca$, respectively, were taken from a previous work by the authors.[9] The following parameters were refined: scale-factors, zero-point, six coefficients of the shifted Chebyshev function to fit the background, unit cell parameters, one Gaussian (G_W, an angle-independent term) and two Lorentzian (L_X and L_Y) terms for profile coefficients, and peak correction for asymmetry.

The crystalline domain size distributions, as well as the average domain sizes of the NPs, were also obtained from XRPD data, collected using the same instrument, but in the 20-115 °2θ range, with a virtual step scan of 0.1 °2θ, and virtual time per step of 500 s. These were analysed *via* the whole powder pattern modelling (WPPM) method,[36] through the PM2K software.[37] This procedure allows us to extract microstructural information from a diffraction pattern, by refining model parameters *via* a non-linear least squares routine so as to fit the experimental peaks, without any use of arbitrary analytical functions (*i.e.* Gaussian, Lorentzian, or Voigtian), as the diffraction peak profile is the result of a convolution of instrumental and sample-related physical effects. In this way, the analysis is assessed taking into account physical models of microstructure and/or lattice defects.[38,39] Basically, with the WPPM method, aspects of microstructure such as the crystalline domain shape and size distribution can be truly assessed, with a method greatly superior to the estimations made by other frequently used integral breadth methods for line profile analysis (LPA), such as the routinely used Scherrer formula[40] or the Williamson–Hall method.[41] In fact, with the use of these other methods,[40,41] it can be cumbersome to correctly extract integral breadths, because of the instrumental profile component, background and peak profile overlapping. Furthermore, additional sources of line broadening – *i.e.* domain size, and / or lattice strain – cannot be considered properly by LPA methods.[42]

The instrumental contribution was obtained by modelling 14 *hkl* reflections from the NIST SRM 660b standard (LaB_6), according to the Caglioti *et al*. relationship.[43] Afterwards, anatase (SG $I4_1/amd$), rutile (SG $P4_2/mnm$) and, when present, brookite (SG $Pbca$), were included in the WPPM modelling. The following parameters were refined: background (modelled using a 4th-order of the shifted Chebyshev polynomial function), peak intensities, specimen displacement, and lattice parameters. In this work, we assumed crystalline domains to be spherical, and distributed according to a lognormal size distribution.

HR-TEM analysis was also assessed using a JEOL 2200FS (JEOL, JP) equipped with an energy dispersive X-ray spectroscopy (EDS) attachment (Oxford Instruments, UK). Samples were prepared by dispersing the nanoparicles in IPA, and evaporating a drop of the suspension on carbon-coated copper grids.

Results and discussion

Quantitative phase analysis (QPA)

As already stated in the introduction, this was an *ex-situ* XRPD preliminary study. Although it is not possible to obtain an accurate kinetic model with the available *ex-situ* data, we can propose a semi-quantitative comparison of the ART transformation kinetics, and define which acid, amongst those employed as counter-ions in the sol (HNO_3, HCl or HBr), delays / accelerates the ART of titania synthesised with this nanosynthesis procedure.

XRPD patterns of the dried gels, as well as of the thermally treated powders at the different temperatures, are depicted in Figs. 1-3. QPA data are reported in Tables 1-3; a graphic output of a Rietveld refinement, sample HCl 450/4h, is shown in Fig. S1 of the electronic supplementary information (ESI, †).

At the drying temperature, 75 °C, the Cl^- counter-ion system contained the least amount of rutile (0.2 wt%), but also the least amount of anatase and the highest level of brookite (47.5, and 20.4 wt%, respectively), of the systems investigated. The amorphous amount, on the other hand, was roughly equal, regardless of the counter-ion used (*cf* Tables 1-3). The presence of brookite is to be expected, as the pH of the sol is acidic (~1).[44–46] Moreover, our findings are contrary to those of Bischoff and Anderson, who stated that a sol acidified with HNO_3 and HCl and peptised at room temperature led to the formation of rutile.[47] Yang *et al*. also found rutile with high specific surface area by peptising sol-gel-derived TiO_2 precipitates with HNO_3, and although at a relatively low hydrothermal synthesis temperature of 200 °C,[48] this was still under conditions very different to our sols dried at 75 °C at atmospheric pressure.

Giving thermal energy to these systems, with a 450 °C isotherm, generally led to a partial crystallisation of the amorphous content (Fig. 4, HR-TEM), but also different crystallisation behaviour depending on the counter-ion used (*i.e.* thermal treatment at 450 °C led to a complete change of the kinetics of the transformation).

With HNO_3 at 450 °C, the amorphous phase crystallised into rutile and brookite, their absolute amounts increasing (respectively: 14.8 and 18.5 wt% at 2 h dwell time). However, while the rutile amount increased with longer dwell times (to 21.1 wt% at 8 h), the amount of brookite decreased, indicating a partial transformation of this polymorph into rutile. Some anatase also transformed into rutile, with a decreased amount at 450 °C compared to HNO_3 75, although further crystallisation of anatase from the amorphous phase cannot be excluded *a priori*, and there is little change in the amount of anatase with

dwell time. Increasing the dwell time to 4 and 8 h (Table 1) continued the ART, and, with the available data, it would appear that the brookite, amorphous, and to a very small amount anatase, phases have all been reduced and transformed into rutile.

The HCl system produced a very different behaviour (Table 2), although the amount of crystallised amorphous phase is comparable (17.3 wt% with HNO_3 *Vs.* 16.0 wt% with HCl after 450 °C / 2 h). The ART has progressed further at 450 °C with a lower amount of anatase, there being only 35.7 wt% after 2 h dwell time, although longer dwell times also led to a partial crystallisation of anatase from the amorphous phase, with its amount increased to 39.8 wt% after 8 h. Brookite exhibited a similar trend to that seen with HNO_3, its amount increasing after 450 °C / 2 h (crystallisation from amorphous), but then decreasing again with longer dwell times, indicating a transformation to rutile. The rutile amount steadily increased both temperature − from 0.2 wt% at 75 °C, to 25.5 wt% at 450 °C / 2 h − and with dwell time, to 32.7 wt% after 450 °C / 2 h.

The HBr system (Table 3) had a different behaviour to both HNO_3 and HCl. This was the sample with the highest starting rutile amount at 75 °C (3.5 wt%). At 450 °C / 2 h, all three crystalline phases has increased in amount, and kept on progressively crystallising with increasing dwell time, at the expense of the amorphous phase. After 450 °C / 8 h, the phase composition was: 58.9 wt% anatase, 16.2 wt% rutile (lowest amount for the counter-ions at this temperature), 16.5 wt% brookite, and 8.5 wt% amorphous phase. Hence, Br^- was the most effective amongst the counter-ions used in delaying the ART at this isotherm, although this sample had the highest starting amount of rutile.

At the 600 °C isotherm (Fig. 3a-c), the brookite → rutile phase transformation is completed in all the systems. With HNO_3, more than one-third of the initial amorphous phase had transformed into rutile, leaving 11.9 wt% after 600 °C / 2 h and only 5.9 wt% after 8 h. Moreover, the ART progressed well, the anatase amount being equal to 21.8 wt% after 2 h and only 10.0 wt% after 8 h, while the amount of rutile has increased to 66.4 wt% after 2 h and 84.1 wt% after 8 h.

For the HCl system at 600 °C, with 2 h dwell time, almost 15 wt% anatase has crystallised into rutile, while after 4 h the amount of anatase has increased from 21.0 to 29.7 wt%, with concomitant loss of amorphous phase, and little change in rutile. Keeping the samples at 600 °C / 8 h led to a further loss of amorphous phase (to 5.1 wt%), as well as crystallisation of anatase into rutile, giving 18.4 and 76.5 wt% of these two phases, respectively.

With HBr, 600 °C / 2 h crystallised all the brookite phase and almost half of the anatase into rutile (61.8 wt%), together with a small amount of the amorphous phase. Upon increasing the dwell time to 4 and 8 h, both anatase and amorphous phases kept on transforming into rutile, as seen with HNO_3 but unlike HCl. There was a particularly large transformation of anatase (from 23.1 to 9.0 wt%) to rutile (from 69.7 to 86.5 wt%) between periods of 4 and 8 h at 600 °C, and sample HBr 600/8h contained 4.5 wt% amorphous phase.

At 800 °C (Fig. S2†), the ART had completed in all three systems, leaving only small amounts of residual amorphous phase with 2 h dwell time (7.4, 5.2, and 4.8 wt% for HNO_3, HCl, and HBr, respectively). Increasing the dwell time just led to a progressive crystallisation of the amorphous phase into rutile for all the samples, until it has virtually disappeared at 8 h dwell time (*cf* Tables 1-3).

Microstructural analysis

WPPM data are shown in Tables 4-6, and Figs 5-8; a graphic output for HNO_3 600/4h is depicted in Fig. S3†. The average crystalline domain diameter of anatase in the dried sols was virtually the same for all the counter-ions used, being 3.3, 3.2, and 3.5 nm for HNO_3 75, HCl 75 and HBr 75, respectively (Fig. 5a-c). Moreover, at this temperature, anatase also had a narrow size distribution, the mode being 3.1, 3.0, and 3.4 nm for HNO_3 75, HCl 75 and HBr 75, respectively. At the same time, the smallest detected crystalline domains had diameters ranging from 1.4 to 2.4 nm, respectively, while the largest ones had a diameter ranging from 5.3 nm (HBr 75) to around 8 nm (HNO_3 and HCl 75), *cf* inset of Fig. 5a-c. On the contrary, both rutile and brookite all had wider size distributions at 75 °C (Tables 4-6). A "critical size" mechanism for the ART has been widely reported in the literature.[14,18,49–51] Zhang and Banfield stated that, for particle size <11 nm, anatase was the thermodynamically stable TiO_2 polymorph;[14] Reidy *et al*. reported that critical size to be around 45 nm.[50] On the other hand, more recently Sabyrov *et al*.[51] postulated that compact anatase aggregates of 3.7 nm diameter particles had a faster ART compared to anatase aggregates of 3.1 nm particles. With the available data presented here (actual amounts of crystalline fractions and their size distributions), we do not wish to comment on any "critical size" mechanism. Actually, after nucleation smaller anatase crystalline domains can dissolve, with larger ones growing at the expense of smaller ones through Ostwald ripening,[52,53] or they can grow through the combination of primary particles into larger secondary ones.[54,55] Moreover, at the 75 °C drying temperature, both brookite and rutile always had smaller detected crystalline domains than anatase (see inset of Fig. 5a-c). As anatase is the thermodynamically stable polymorph at the nanoscale,[14] and the pH of the sols was strongly acidic (pH ~1), we can argue that:

- brookite formed together with anatase, due to the pH of the sol being around 1, as it is known that the brookite amount increases with increasing sol pH in the range of 0.5 < pH < 3);[46,59] then dissolution of anatase or brookite took place (brookite crystals are more soluble than anatase ones), to form brookite or rutile.
- both brookite and rutile formed at the 75 °C drying step, due to anatase nanoparticle dissolution,[51] with subsequent formation of rutile and brookite. In this regard, brookite is known to increase solubility and act as a rutile nucleation site.[56–58]

At 450 °C, there was obviously a progressive increase in the average crystalline domain diameters of anatase, rutile and

brookite with dwell time (Figs 6-8). With HNO_3 and HCl as counter-ions, the anatase average domain diameter was three times higher at 2 h dwell time, compared to the size at the 75 °C drying temperature. However, with HBr, anatase did not even double its size (*e.g.* 3.5 nm at 75 °C *vs.* 6.1 nm at 450 °C/ 2 h) Interestingly, at this isotherm, the smaller the average anatase domain diameter, the higher its proportion in the sample (*i.e.* 6.1 nm and 55.6 wt% in HBr 450 °C/ 2 h), this qualitatively indicating less anatase growth, and thus a lower ART rate with HBr. Also, rutile increased in size following an opposite trend compared to anatase: the smaller its average size, the smaller its amount in the sample (HBr < HNO_3 < HCl), thus supporting the statement of a lower ART rate. Together with the progress of the ART and the particle size growth, the amorphous phase also continued to crystallise. This crystallisation is evident from the wide size distribution, and the small sizes, of the minimum detected crystalline domains (*cf* Tables 1-3, and inset of Figs 6-8) in all the three titania polymorphs, in all three systems.

The 600 °C isotherm qualitatively gave the similar information around the microstructure as the 450 °C isotherm, but with different trends (Figs S4-S6†). The HBr system had the highest amount of anatase at 600 °C / 2 h (27.5 wt%), but it also had the largest average crystalline domain diameter (25.8 nm, *vs.* 24.3 nm for HNO_3 600/2h and 20.9 nm for HCl 600/2h). However, after 600 °C / 8 h, the HBr sample had the lowest anatase content (9.0 wt%), compared to HCl with the highest content (18.4 wt%), qualitatively indicating a lower ART rate for HCl at that isotherm. This could be seen as indirect evidence of the ART mechanism, often described as a nucleation and growth mechanism. Zhang and Banfield suggested that, for nanocrystalline anatase, rutile nucleation might start within the interface between two contacting anatase particles; after that, a stable rutile nucleus is born, and the formation of rutile particles is prompted.[20,21] The larger anatase particles seen in the HBr sample may be superior nuclei for rutile formation.

At the isotherm of 800 °C (Fig. S7†), the ART is fully accomplished in all the samples. Following the nucleation and growth mechanism, the rutile mean crystalline domain size keeps on increasing, reaching the sub-micrometric range after 4 h dwell time, accompanied by a narrowing of the size distribution (*e.g.* when the average crystalline domain diameter is > 90 nm).

Lattice volume expansion

Data describing the unit cell parameters and volumes of the TiO_2 polymorphs in the samples are shown in Tables 7-9. For titania polymorphs in the dried sols at 75 ºC, the error is relatively high due to its poor crystallinity. If we consider the data for rutile in the samples that underwent a thermal treatment at 450 and 600 °C for all three dwell times, we observe an inverse linear relationship between the lattice volume expansion and the increase of crystalline domain size for rutile (Fig. 9a-c). In other words, for the same system (*e.g.* the counter-ion used), as the average crystalline domain diameter increases in the same isotherm with dwell time (as 1/D decreases), the unit cell contracts (see Fig. 9a,b). The extent of this phenomenon depends on the counter-ion used. When rutile crystals have become much larger (approximately >90 nm, *i.e.* only with 4 and 8 h dwell time) at the isotherm of 800 °C, this relationship reverses and becomes a direct linear relationship between increase in cell volume and increase in crystalline domain size (Fig. 9c). In other words, when rutile is still nanocrystalline, there is a linear dependence of the (slight) lattice volume expansion on the decrease of the crystalline domain size, the opposite happening when the rutile crystalline domain diameter becomes sub-micrometric.

A similar inverse relationship has already been reported for several metal oxides – Al_2O_3, CeO_2, Fe_2O_3, HfO_2 – when they are on the nanoscale,[60–64] even if controversial and conflicting explanations have been proposed. Some authors suggested that phenomenon could be caused by a Ti vacancies mechanism in rutile;[65] others attributed it to negative interface pressure,[66] yet others to a surface relaxation phenomenon.[62,63] It does seem from our data that somewhere, approximately at size < 90 nm, there is a critical nanocrystalline domain size for rutile, above which this inverse relationship does not exist, and is replaced by a direct linear relationship between crystalline domain size and unit cell volume (*cf* Fig. 9c). This results in the reversal of gradient seen in Figs 9a,b.

For anatase, we observed no linear dependence of lattice parameters with crystalline domain size, either inverse or direct (data not reported here), hence contrasting with what was seen for rutile. More experimental work is needed, and is currently being undertaken, to fully understand such peculiar behaviour.

Conclusions

TiO_2 nanopowders have been synthesised *via* an aqueous sol-gel method, using three different mineral acids (HNO_3, HBr and HCl) to peptise the sol, and thus provide counter-ions. The effects of sol counter-ions on the phase composition and microstructure of the thermally treated samples was thoroughly characterised using advanced X-ray powder diffraction methods (*e.g.* Rietveld−RIR and WPPM). With the available *ex-situ* data, we proposed a semi-quantitative comparison of the anatase-to-rutile phase transition (ART) kinetics, defining which acid, supplying counter-ions to the sol, delayed or accelerated the ART. At a low drying temperature of 75 °C, the Cl^- counter-ion was the most favourable one to obtain anatase as the major crystalline phase, delaying the onset of the ART – the corresponding TiO_2 contained only 0.2 wt% rutile. Conversely, the titania containing Br^- ions, had more anatase with larger crystalline domain diameter at the 450 °C isotherm, and hence, a lower ART rate. However, in general, halides were more effective in delaying the ART than NO_3^-

With investigations of the nanostructure by WPPM, we report an inverse linear relationship between unit cell volume and crystalline domain size in rutile TiO_2. For the samples that underwent a thermal treatment at 450 and 600 °C isotherms, we observed an increase in the lattice volume expansion of rutile,

as the crystalline domain size decreased. As the domain sizes increased with temperature this effect decreased, and after thermal treatment at 800 °C resulted in large domains, over 90 nm in size, that relationship was reversed and became a direct linear dependence.

Acknowledgements

D.M. Tobaldi is thankful to the ECO-SEE project (funding from the European Union's Seventh Framework Programme for research, technological development and demonstration under grant agreement no 609234. *Note: The views expressed are purely those of the authors and may not in any circumstances be regarded as stating an official position of the European Commission*). R.C. Pullar acknowledges the support of FCT grant SFRH/BPD/97115/2013. We would also like to be grateful to an anonymous reviewer, who gave us the stimulus to improve the manuscript.

Notes and references

[a] *Department of Materials and Ceramic Engineering / CICECO, University of Aveiro, Campus Universitário de Santiago, 3810-193 Aveiro, Portugal.*
E-mail: david.tobaldi@ua.pt, david@davidtobaldi.org; Tel: +351 234 370 041.
[b] *Dipartimento di Scienze Chimiche e Geologiche, Università degli studi di Modena e Reggio Emilia, I-41121 Modena, Italy.*
[c] *Christopher Ingold Building, Department of Chemistry, University College of London,20 Gordon Street, London, WC1H 0AJ, UK.*
[d] *School of Engineering and Materials Science, Queen Mary University of London, London E1 4NS, UK.*

† Electronic Supplementary Information (ESI) available: [graphic output of the Rietveld refinement, and the WPPM modelling; XRPD patterns of the samples thermally treated at the 800 °C isotherm; size distribution, as obtained from the WPPM modelling, of samples **HNO_3 600**, **HCl 600** and **HBr 600** at the different dwell time used; rutile size distributions at the 800 °C isotherm]. See DOI: 10.1039/b000000x/

References

1 P. V. Kamat, *J. Phys. Chem. Lett.*, 2011, **2**, 839–840.
2 G. Meacock, K. D. A. Taylor, M. J. Knowles and A. Himonides, *J. Sci. Food Agric.*, 1997, **73**, 221–225.
3 B. O'Regan and M. Grätzel, *Nature*, 1991, **353**, 737–740.
4 I. Mora-Seró and J. Bisquert, *J. Phys. Chem. Lett.*, 2010, **1**, 3046–3052.
5 T. Miyasaka, *J. Phys. Chem. Lett.*, 2011, **2**, 262–269.
6 A. Fujishima and K. Honda, *Nature*, 1972, **238**, 37–38.
7 A. Fujishima, K. Hashimoto and T. Watanabe, *TiO2 photocatalysis: fundamentals and applications*, BKC, Tokyo, Japan, 1999.
8 A. Fujishima, T. N. Rao and D. A. Tryk, *J. Photochem. Photobiol. C Photochem. Rev.*, 2000, **1**, 1–21.
9 D. M. Tobaldi, R. C. Pullar, A. F. Gualtieri, M. P. Seabra and J. A. Labrincha, *Acta Mater.*, 2013, **61**, 5571–5585.
10 H. Zhang and J. F. Banfield, *Chem. Rev.*, 2014, **114**, 9613–9644.
11 J. Muscat, V. Swamy and N. Harrison, *Phys. Rev. B*, 2002, **65**.
12 S. J. Smith, R. Stevens, S. Liu, G. Li, A. Navrotsky, J. Boerio-Goates and B. F. Woodfield, *Am. Mineral.*, 2009, **94**, 236–243.
13 A. A. Gribb and J. F. Banfield, *Am. Mineral.*, 1997, **82**, 717–728.
14 H. Zhang and J. F. Banfield, *J. Mater. Chem.*, 1998, **8**, 2073–2076.
15 K.-N. P. Kumar, K. Keizer and A. J. Burggraaf, *J. Mater. Chem.*, 1993, **3**, 1141–1149.
16 J. Ovenstone and K. Yanagisawa, *Chem. Mater.*, 1999, **11**, 2770–2774.
17 J.-G. Li and T. Ishigaki, *Acta Mater.*, 2004, **52**, 5143–5150.
18 T. Mitsuhashi and O. J. Kleppa, *J. Am. Ceram. Soc.*, 1979, **62**, 356–357.
19 S. G. Kumar and K. S. R. K. Rao, *Nanoscale*, 2014, **6**, 11574–11632.
20 H. Zhang and J. F. Banfield, *Am. Mineral.*, 1999, **84**, 528–535.
21 H. Zhang and J. F. Banfield, *J. Mater. Res.*, 2000, **15**, 437–448.
22 Y. Bai, I. Mora-Seró, F. De Angelis, J. Bisquert and P. Wang, *Chem. Rev.*, 2014, **114**, 10095–10130.
23 K. Liu, M. Cao, A. Fujishima and L. Jiang, *Chem. Rev.*, 2014, **114**, 10044–10094.
24 M. Kapilashrami, Y. Zhang, Y.-S. Liu, A. Hagfeldt and J. Guo, *Chem. Rev.*, 2014, **114**, 9662–9707.
25 Y. Ma, X. Wang, Y. Jia, X. Chen, H. Han and C. Li, *Chem. Rev.*, 2014, **114**, 9987–10043.
26 T. Rajh, N. M. Dimitrijevic, M. Bissonnette, T. Koritarov and V. Konda, *Chem. Rev.*, 2014, **114**, 10177–10216.
27 L. Wang and T. Sasaki, *Chem. Rev.*, 2014, **114**, 9455–9486.
28 K. Yanagisawa and J. Ovenstone, *J. Phys. Chem. B*, 1999, **103**, 7781–7787.
29 Q. Zhang, L. Gao and J. Guo, *J. Eur. Ceram. Soc.*, 2000, **20**, 2153–2158.
30 Y. Li, T. J. White and S. H. Lim, *J. Solid State Chem.*, 2004, **177**, 1372–1381.
31 D. M. Tobaldi, R. C. Pullar, A. F. Gualtieri, M. P. Seabra and J. A. Labrincha, *Chem. Eng. J.*, 2013, **214**, 364–375.
32 A. F. Gualtieri, *J. Appl. Crystallogr.*, 2000, **33**, 267–278.
33 A. F. Gualtieri and G. Brignoli, *J. Appl. Crystallogr.*, 2004, **37**, 8–13.
34 A. C. Larson and R. B. Von Dreele, *General Structure Analysis System (GSAS)*, Los Alamos National Laboratory Report LAUR, 2004.
35 B. H. Toby, *J. Appl. Crystallogr.*, 2001, **34**, 210–213.
36 P. Scardi and M. Leoni, *Acta Crystallogr. A*, 2002, **58**, 190–200.
37 M. Leoni, T. Confente and P. Scardi, *Z. Für Krist. Suppl.*, 2006, **23**, 249–254.
38 P. Scardi and M. Leoni, in *Diffraction Analysis of the Microstructure of Materials*, Eric J. Mittemeijer, Paolo Scardi, Berlin, Springer-Verlag., 2004, pp. 51–92.
39 P. Scardi and M. Leoni, *J. Appl. Crystallogr.*, 2006, **39**, 24–31.
40 H. P. Klug and L. E. Alexander, *X-ray diffraction procedures for polycrystalline and amorphous materials*, Wiley, New York, 2nd Edition., 1974.
41 G. K. Williamson and W. H. Hall, *Acta Metall.*, 1953, **1**, 22–31.
42 P. Scardi and M. Leoni, *Acta Mater.*, 2005, **53**, 5229–5239.
43 G. Caglioti, A. Paoletti and F. P. Ricci, *Nucl. Instrum. Methods*, 1960, **9**, 195–198.
44 A. Pottier, C. Chanéac, E. Tronc, L. Mazerolles and J.-P. Jolivet, *J. Mater. Chem.*, 2001, **11**, 1116–1121.

45 Y. Hu, H.-L. Tsai and C.-L. Huang, *J. Eur. Ceram. Soc.*, 2003, **23**, 691–696.
46 S. L. Isley and R. L. Penn, *J. Phys. Chem. B*, 2006, **110**, 15134–15139.
47 B. L. Bischoff and M. A. Anderson, *Chem. Mater.*, 1995, **7**, 1772–1778.
48 J. Yang, S. Mei and J. M. F. Ferreira, *J. Am. Ceram. Soc.*, 2000, **83**, 1361–1368.
49 P. . Gouma, P. . Dutta and M. . Mills, *Nanostructured Mater.*, 1999, **11**, 1231–1237.
50 D. J. Reidy, J. D. Holmes and M. A. Morris, *J. Eur. Ceram. Soc.*, 2006, **26**, 1527–1534.
51 K. Sabyrov, N. D. Burrows and R. L. Penn, *Chem. Mater.*, 2013, **25**, 1408–1415.
52 G. Oskam, Z. Hu, R. Penn, N. Pesika and P. Searson, *Phys. Rev. E*, 2002, **66**.
53 L. Ratke and P. W. Voorhees, *Growth and coarsening: Ostwald ripening in material processing*, Springer, Berlin; New York, 2002.
54 R. L. Penn and J. F. Banfield, *Geochim. Cosmochim. Acta*, 1999, **63**, 1549–1557.
55 J. Park, V. Privman and E. Matijević, *J. Phys. Chem. B*, 2001, **105**, 11630–11635.
56 R. L. Penn and J. F. Banfield, *Am. Mineral.*, 1998, **83**, 1077–1082.
57 R. L. Penn and J. F. Banfield, *Am. Mineral.*, 1999, **84**, 871–876.
58 H. Zhang and J. F. Banfield, *J. Phys. Chem. B*, 2000, **104**, 3481–3487.
59 S. L. Isley and R. L. Penn, *J. Phys. Chem. C*, 2008, **112**, 4469–4474.
60 P. Ayyub, V. Palkar, S. Chattopadhyay and M. Multani, *Phys. Rev. B*, 1995, **51**, 6135–6138.
61 S. Tsunekawa, K. Ishikawa, Z.-Q. Li, Y. Kawazoe and A. Kasuya, *Phys. Rev. Lett.*, 2000, **85**, 3440–3443.
62 M. Leoni and P. Scardi, in *Diffraction Analysis of the Microstructure of Materials*, Eric J. Mittemeijer, Paolo Scardi, Berlin, Springer-Verlag., 2004, pp. 413–454.
63 M. Leoni, *Mater. Sci. Forum*, 2004, **443-444**, 1–10.
64 C. V. Ramana, K. K. Bharathi, A. Garcia and A. L. Campbell, *J. Phys. Chem. C*, 2012, **116**, 9955–9960.
65 A. Y. Kuznetsov, R. Machado, L. S. Gomes, C. A. Achete, V. Swamy, B. C. Muddle and V. Prakapenka, *Appl. Phys. Lett.*, 2009, **94**, 193117.
66 G. Li, J. Boerio-Goates, B. F. Woodfield and L. Li, *Appl. Phys. Lett.*, 2004, **85**, 2059.

Figures & Captions

Fig. 1 – XRPD patterns of the samples dried at 75 °C. The vertical bars represent the XRPD peaks of anatase (blue, JCPDS-PDF card no. 21-1272), rutile (red, JCPDS-PDF card no. 21-1276), and brookite (green, JCPDS-PDF card no. 29-1360 – only the four most intense reflections were reported here).

Fig. 2 – XRPD patterns of the samples after being thermally treated at the 450 °C isotherm. a) **HNO_3**; b) **HCl**; c) **HBr** as sources of counter-ions. The vertical bars represent the XRPD peaks of anatase (blue, JCPDS-PDF card no. 21-1272), rutile (red, JCPDS-PDF card no. 21-1276), and brookite (green, JCPDS-PDF card no. 29-1360 – only the four most intense reflections were reported here).

Fig. 3 – XRPD patterns of the samples after being thermally treated at the 600 °C isotherm. a) **HNO_3**; b) **HCl**; c) **HBr** as sources of counter-ions. The vertical bars represent the XRPD peaks of anatase (blue, JCPDS-PDF card no. 21-1272), rutile (red, JCPDS-PDF card no. 21-1276), and brookite (green, JCPDS-PDF card no. 29-1360 – only the four most intense reflections were reported here).

Fig. 4 – HR-TEM micrographs of samples: a) **HNO_3 450/2h**, and b) **HBr 450/2h**, highlighting a halo of amorphous phase around TiO_2 nanoparticles. c) Magnification of the selected area shown in b).

Fig. 5 – Size distribution, as obtained from the WPPM modelling, of samples dried at **75 °C**, using: a) **HNO_3**; b) **HCl**; c) **HBr** as sources of counter-ions. Insets report a magnification so as to highlight the tails of anatase size distribution.

Fig. 6 – Size distribution, as obtained from the WPPM modelling, of sample **HNO_3 450** at different dwell time. a) anatase; b) rutile; c) brookite. The inset shows a magnification in order to highlight the minimum crystalline domain diameter detected.

Fig. 7 – Size distribution, as obtained from the WPPM modelling, of sample **HCl 450** at different dwell time. a) anatase; b) rutile; c) brookite. The inset shows a magnification in order to highlight the minimum crystalline domain diameter detected.

Fig. 8 – Size distribution, as obtained from the WPPM modelling, of sample **HBr 450** at different dwell time. a) anatase; b) rutile; c) brookite. The inset shows a magnification in order to highlight the minimum crystalline domain diameter detected.

Fig. 9 – Crystalline domain size dependence of the unit cell volume, for rutile, in the samples. a) 450 °C isotherm; b) 600 °C isotherm; c) 800 °C isotherm.

Fig. 1

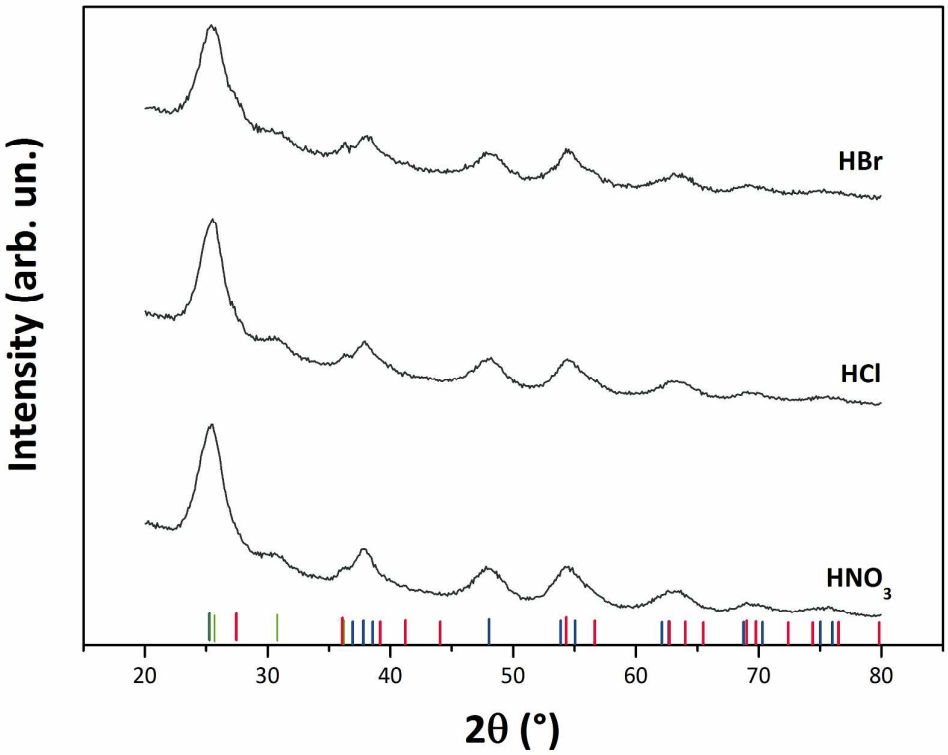

Fig. 2a

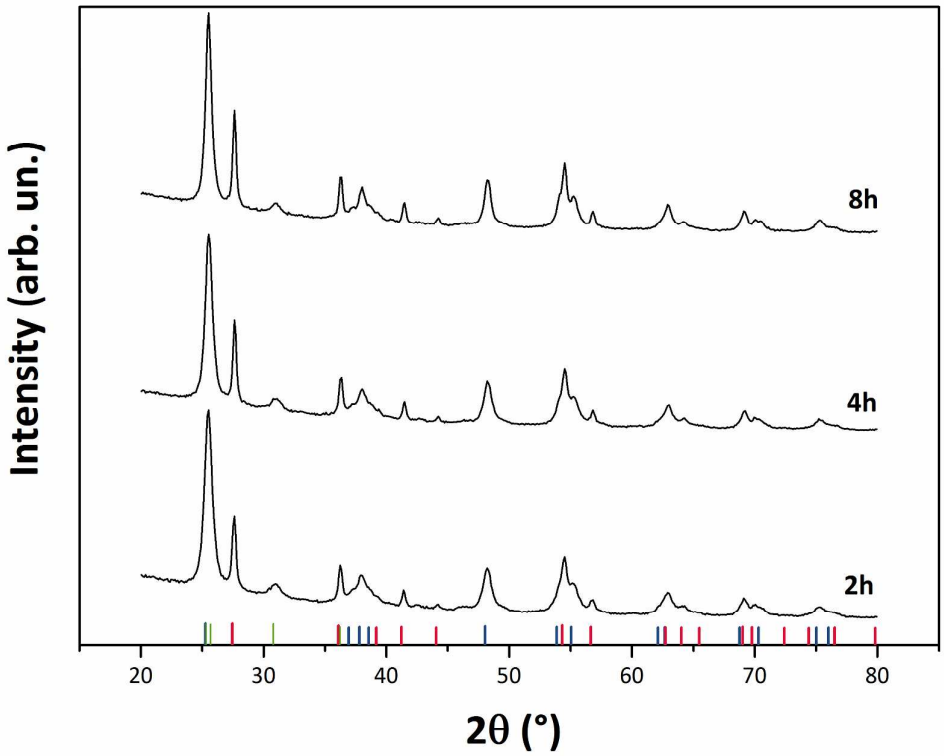

Fig. 2b

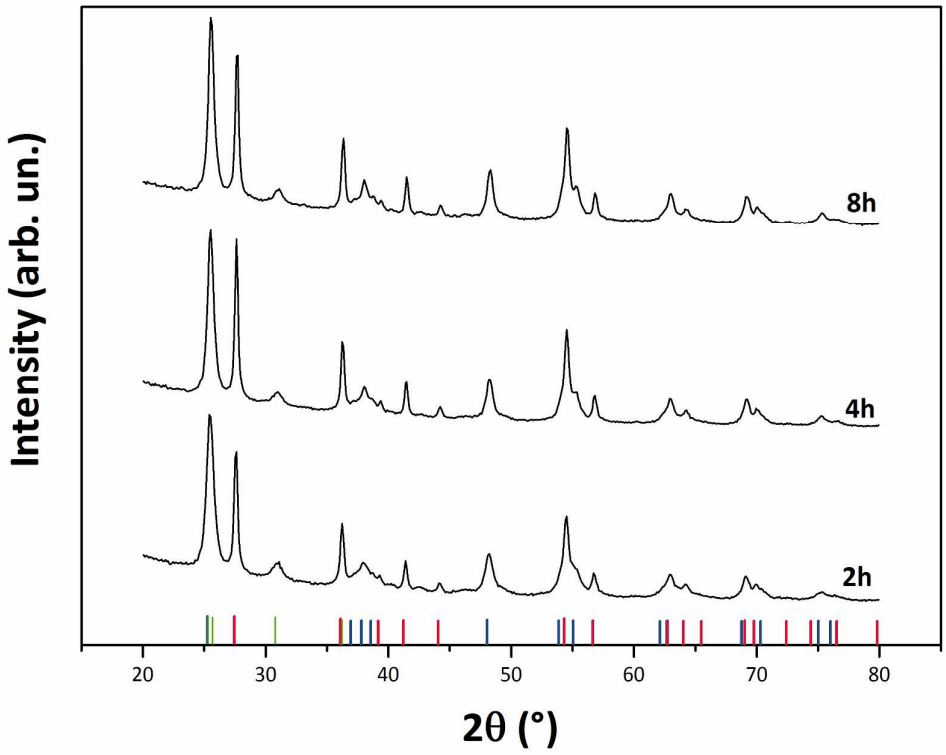

Fig. 2c

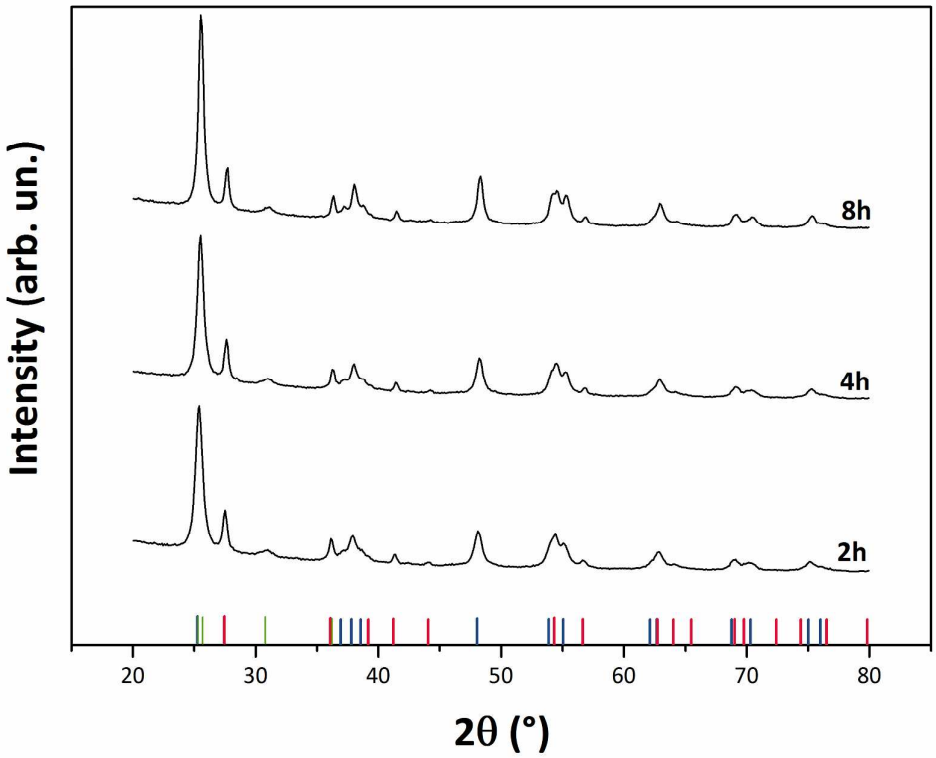

Fig. 3a

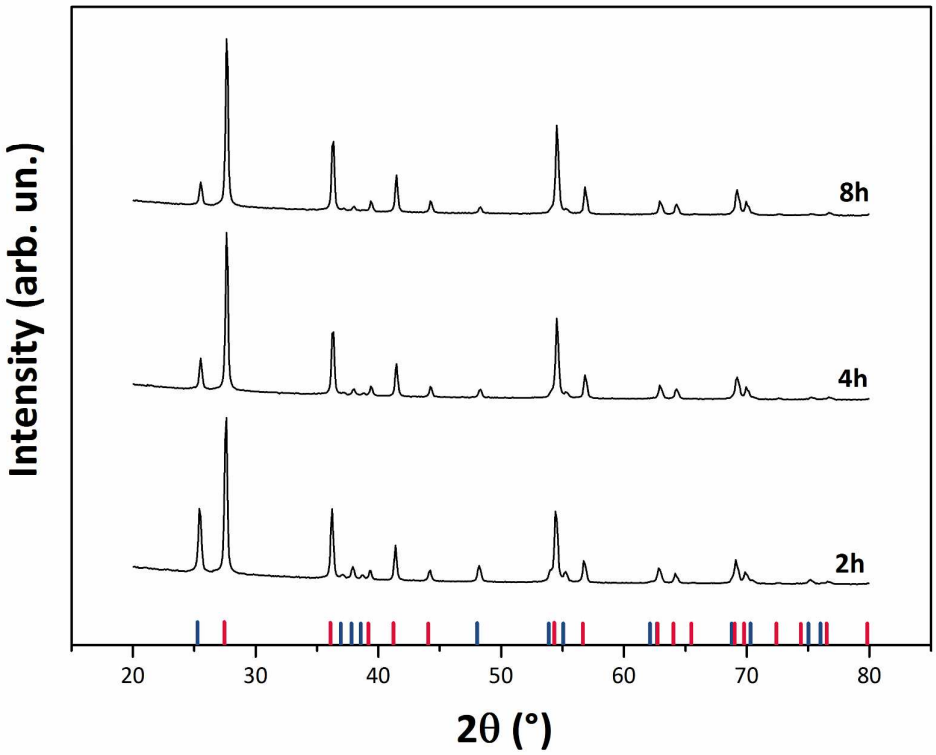

Fig. 3b

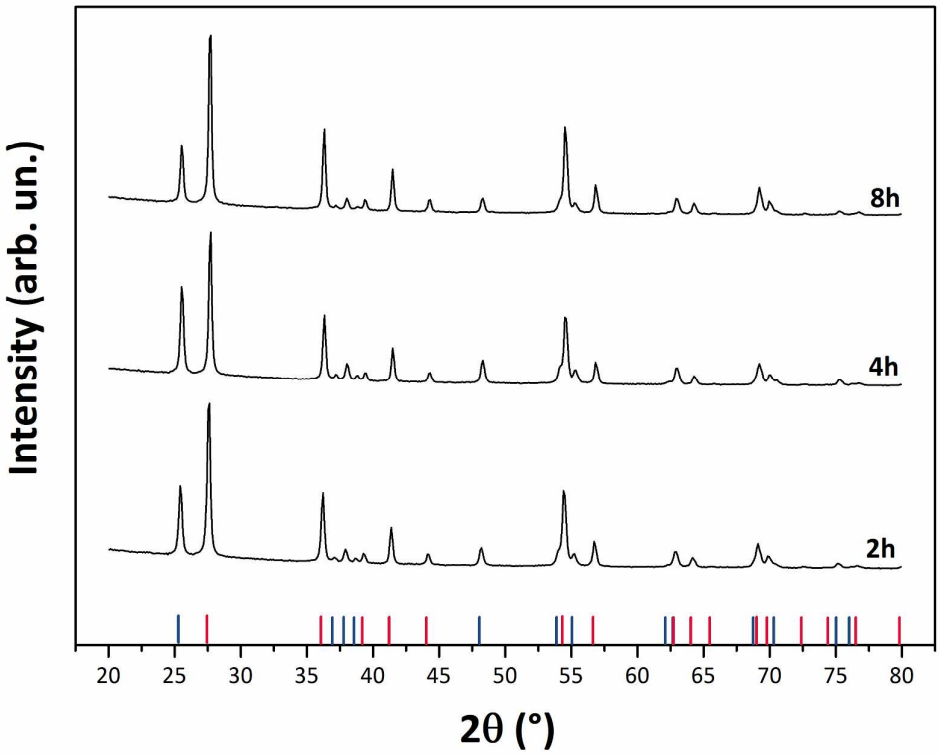

Fig. 3c

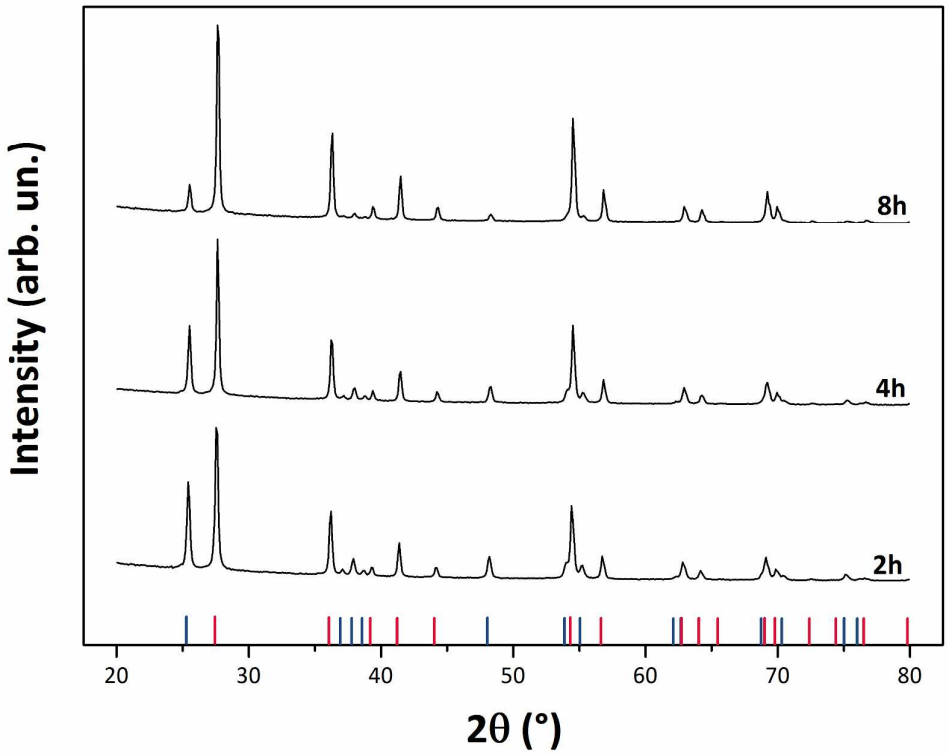

Fig. 4a

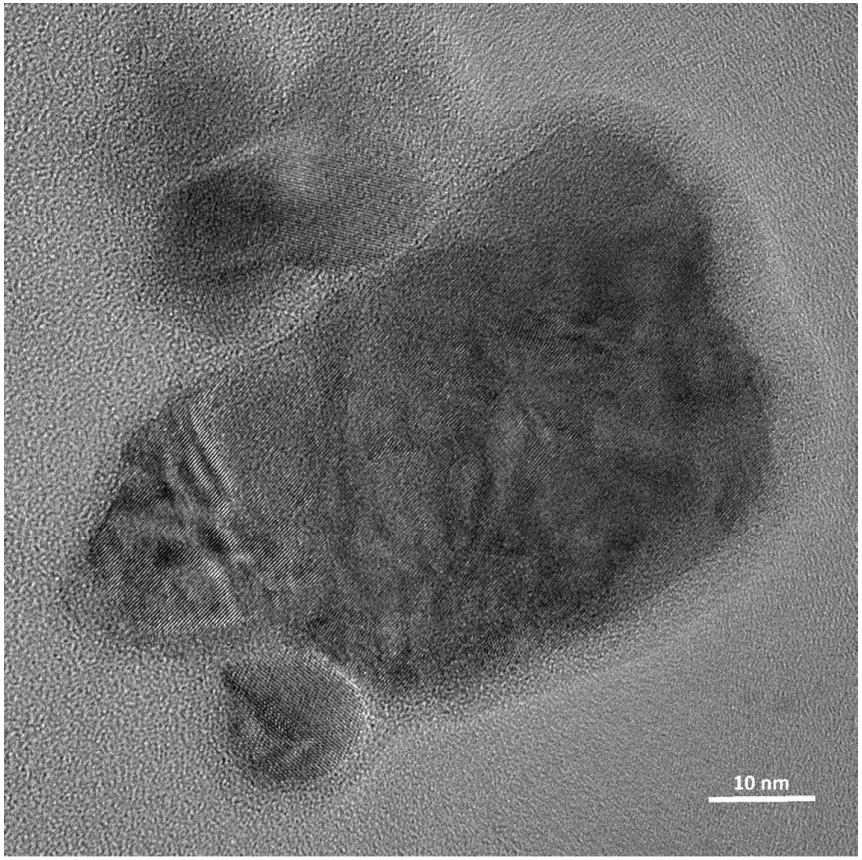

Fig. 4b

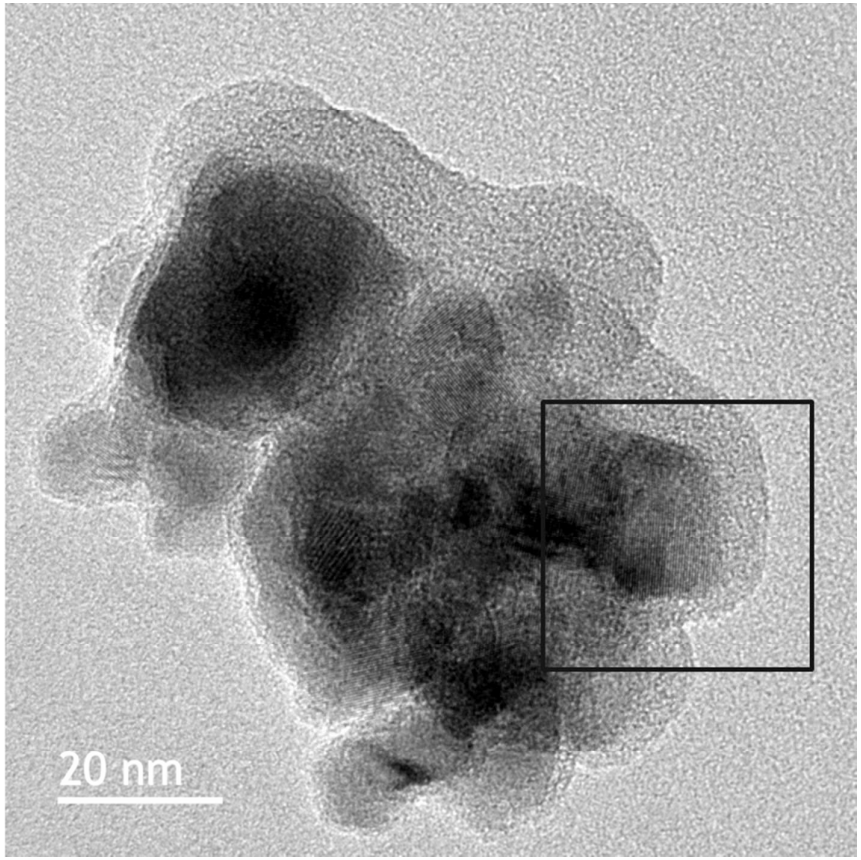

Fig. 4c

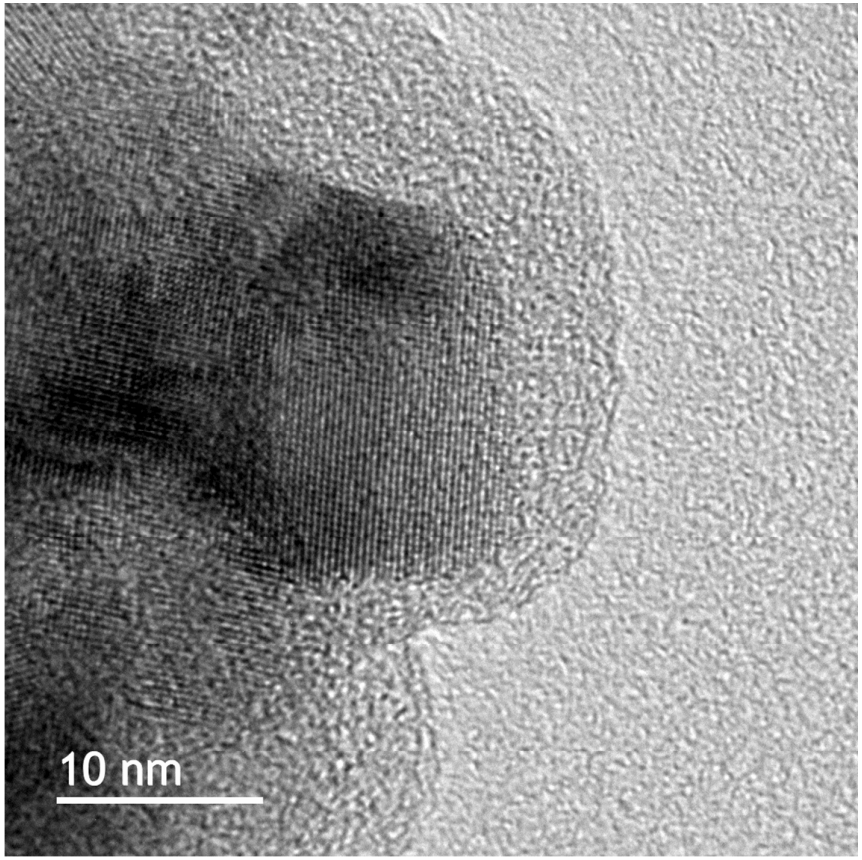

Fig. 5a

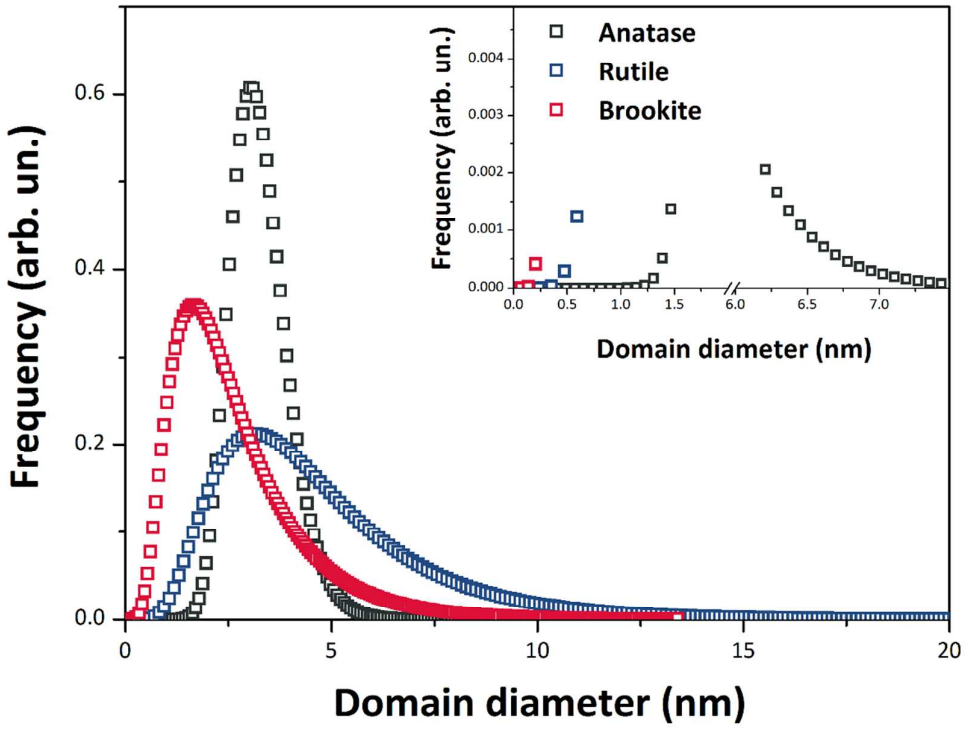

Fig. 5b

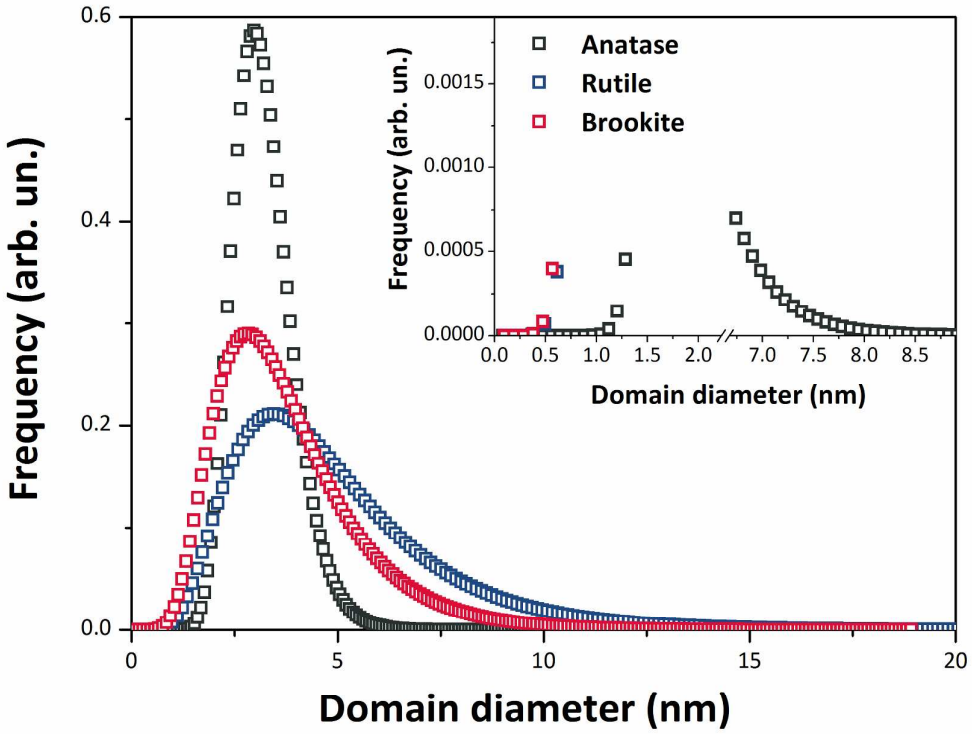

Fig. 5c

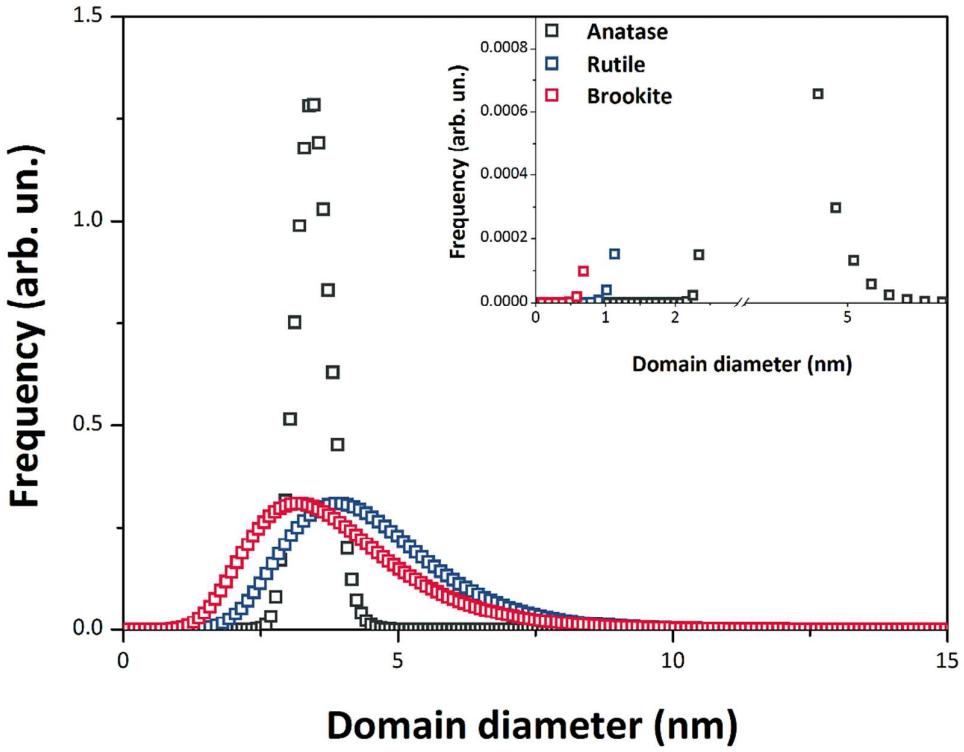

Fig. 6a

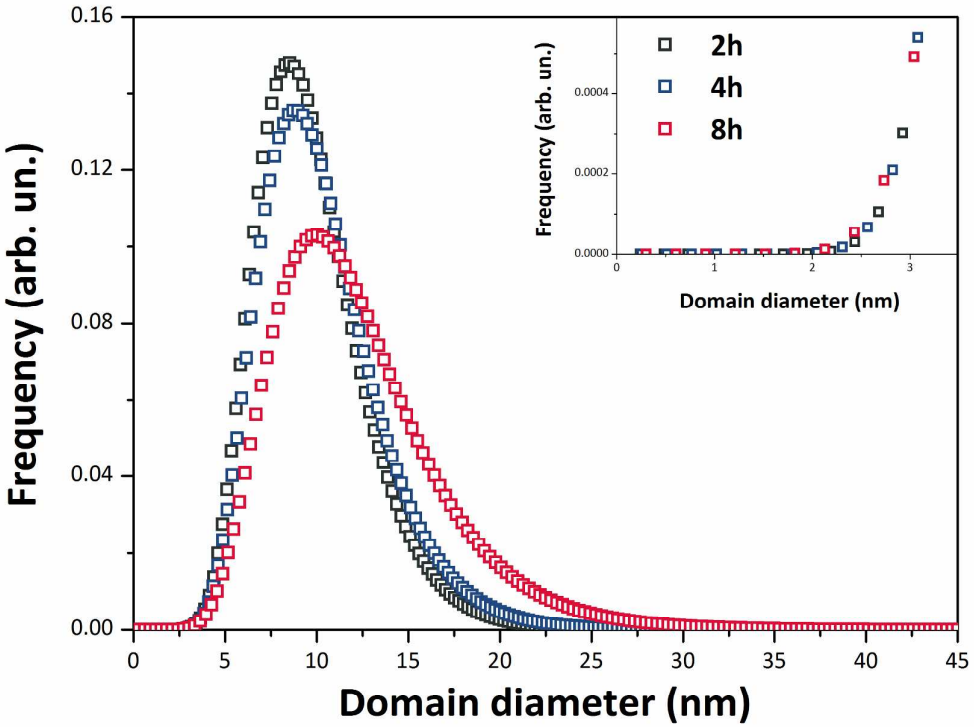

Fig. 6b

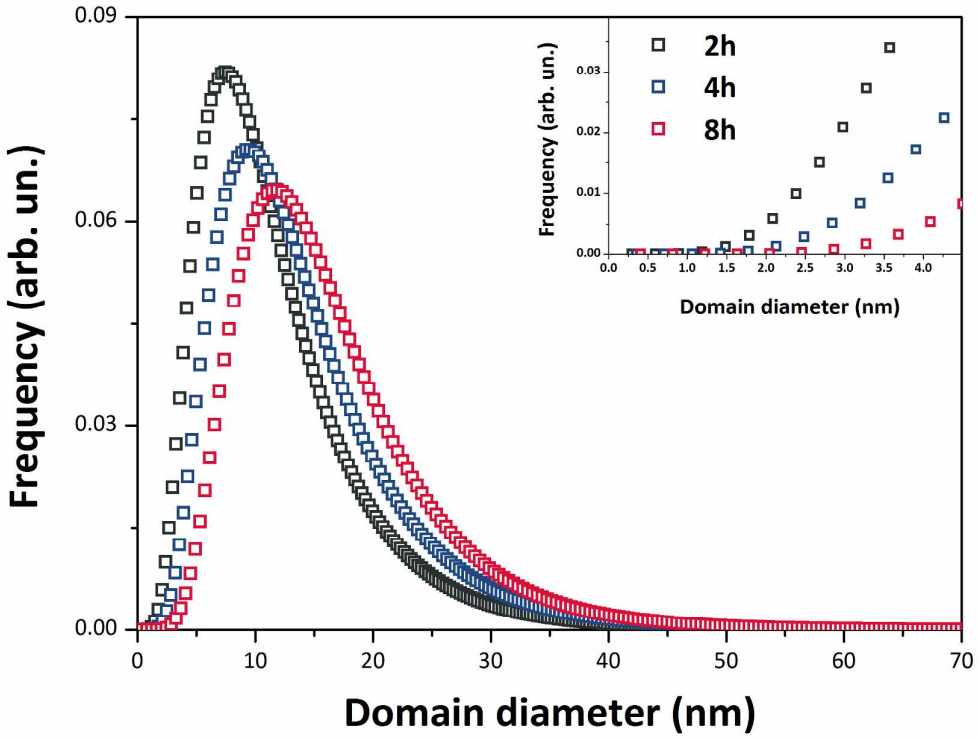

Fig. 6c

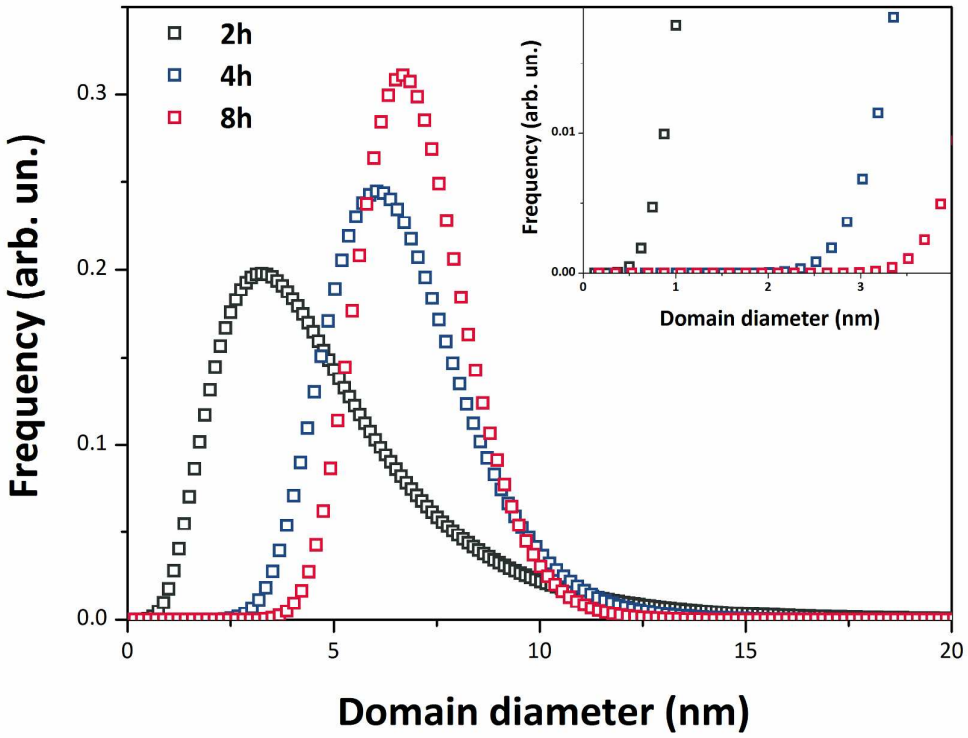

Fig. 7a

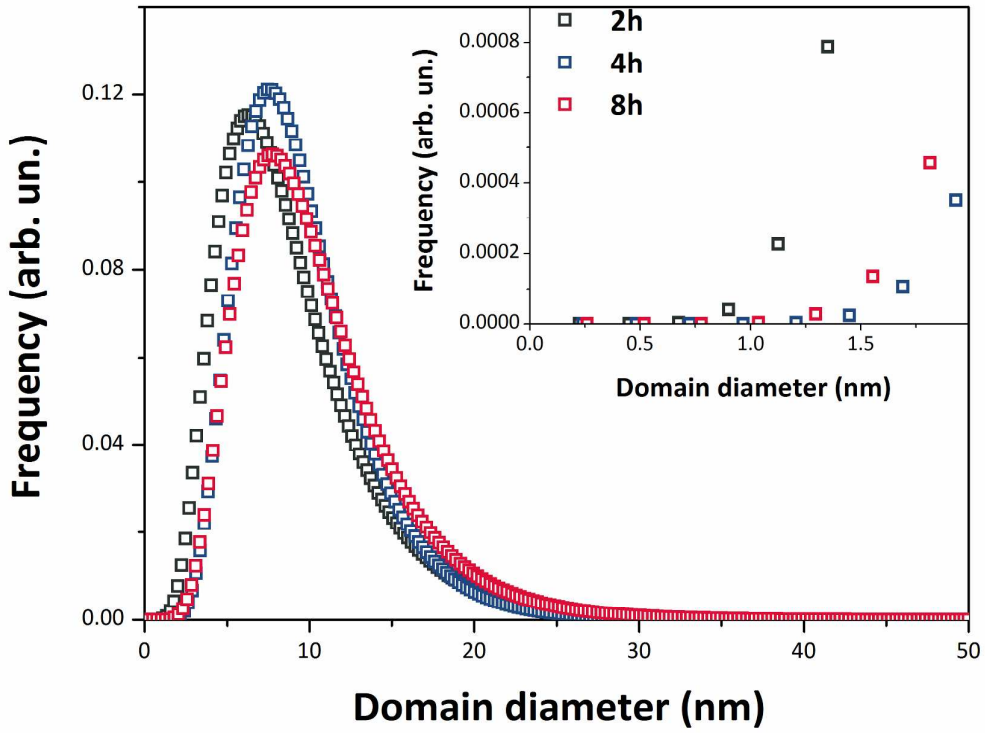

Fig. 7b

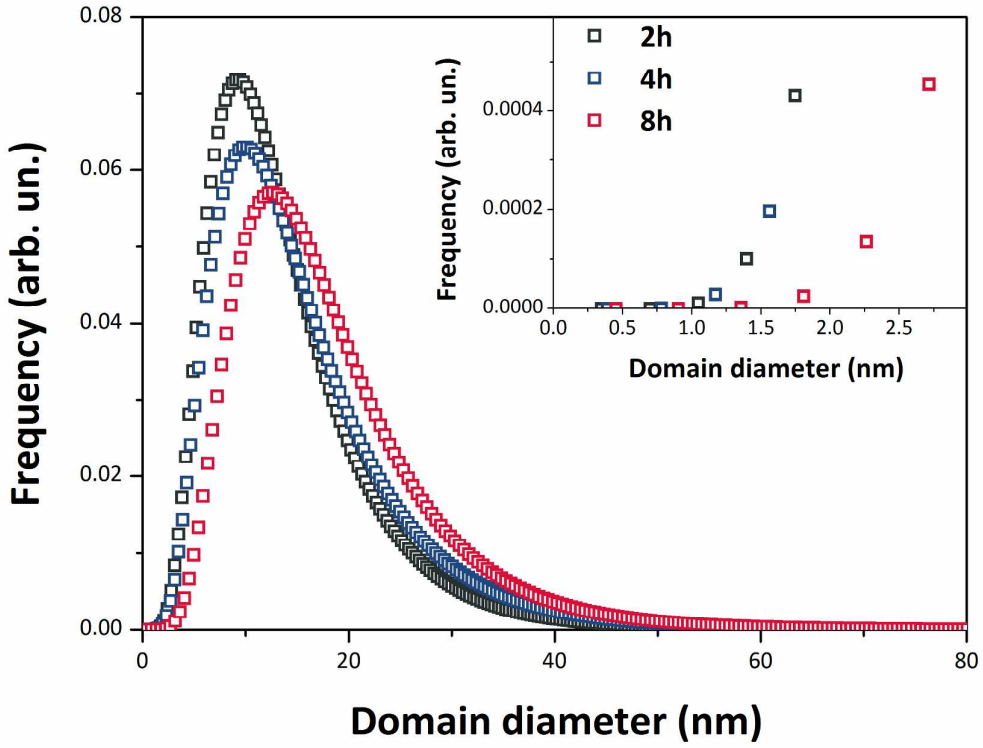

Fig. 7c

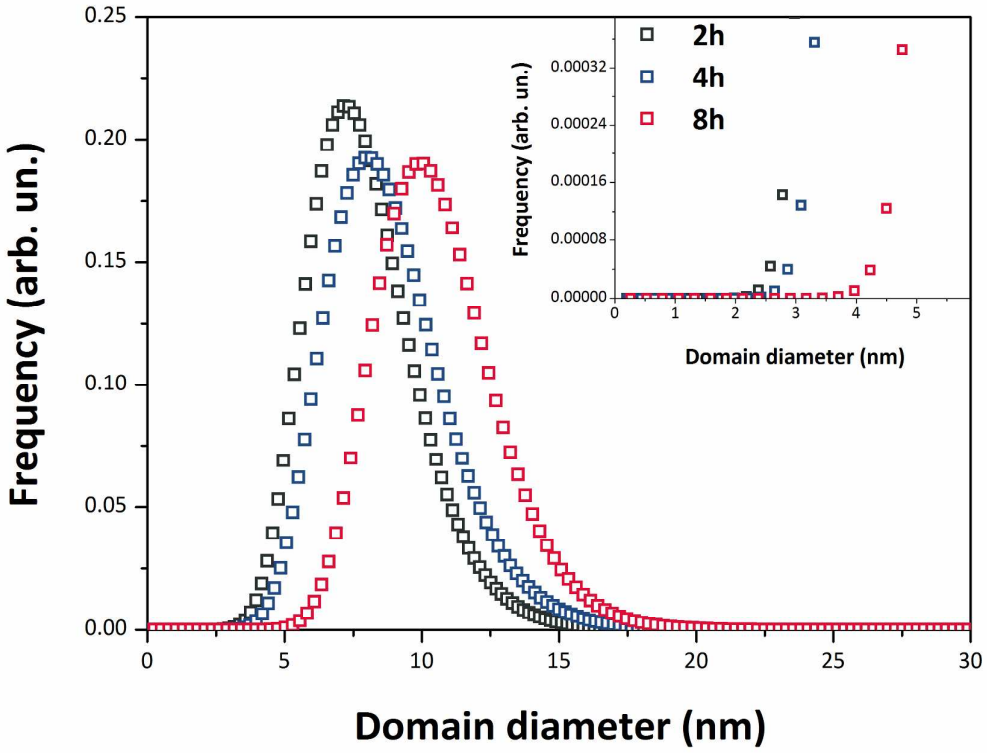

Fig. 8a

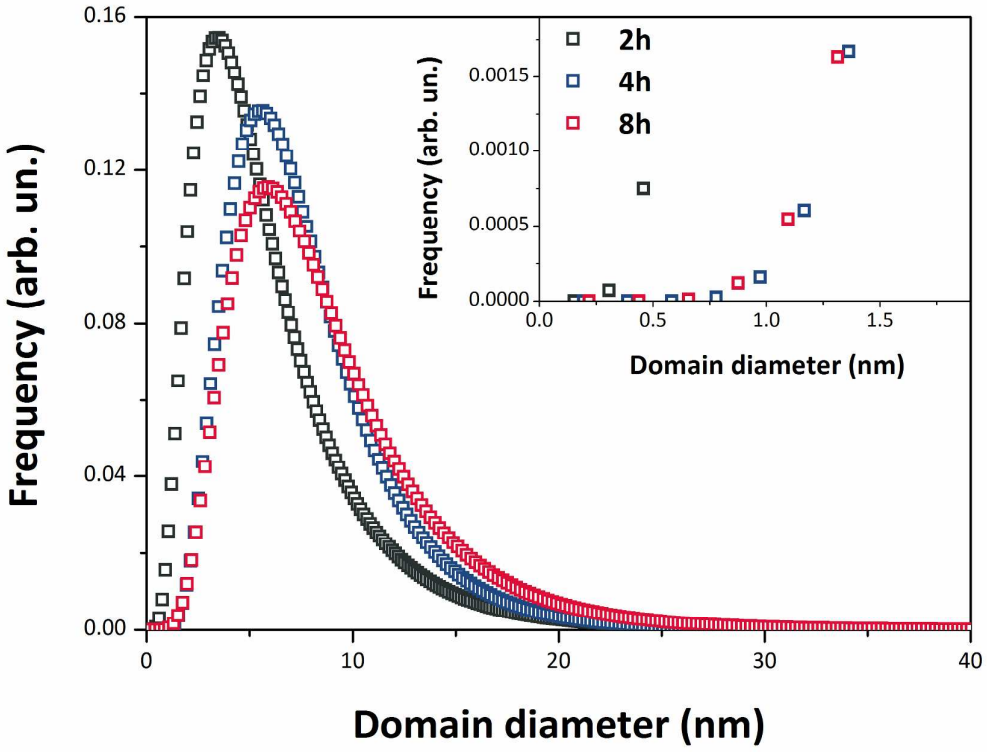

Fig. 8b

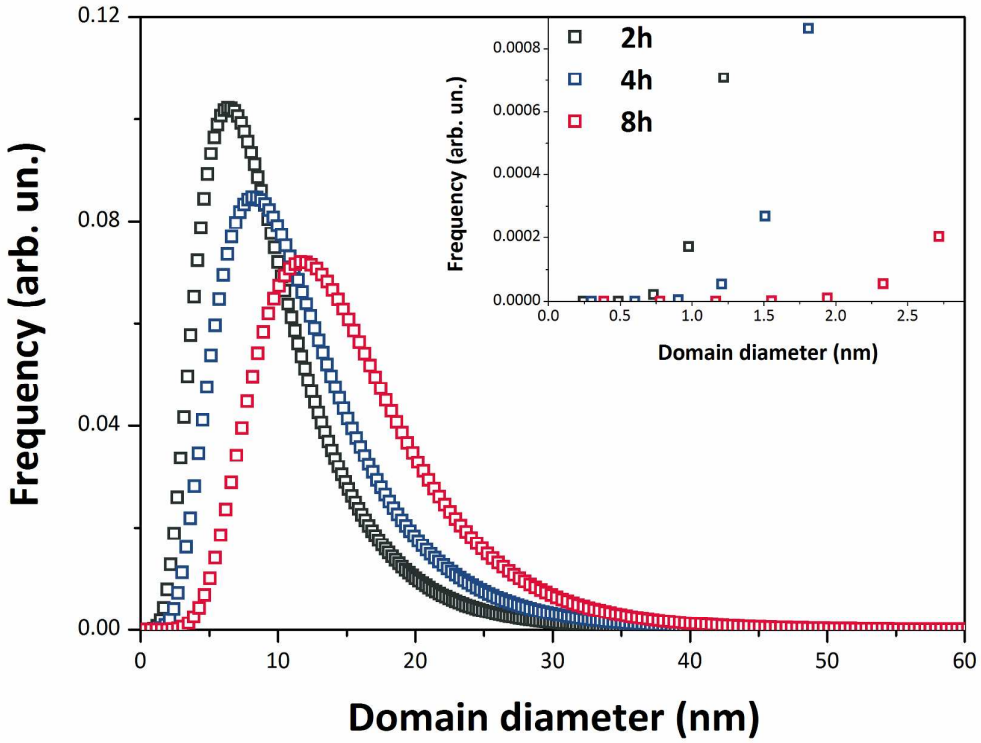

Fig. 8c

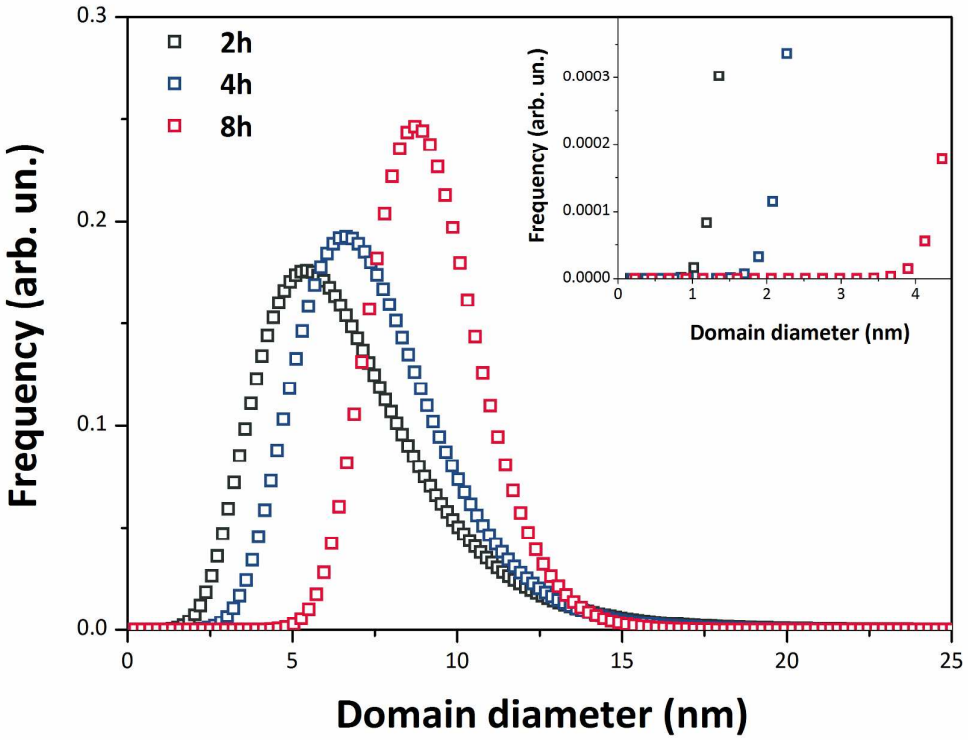

Fig. 9a

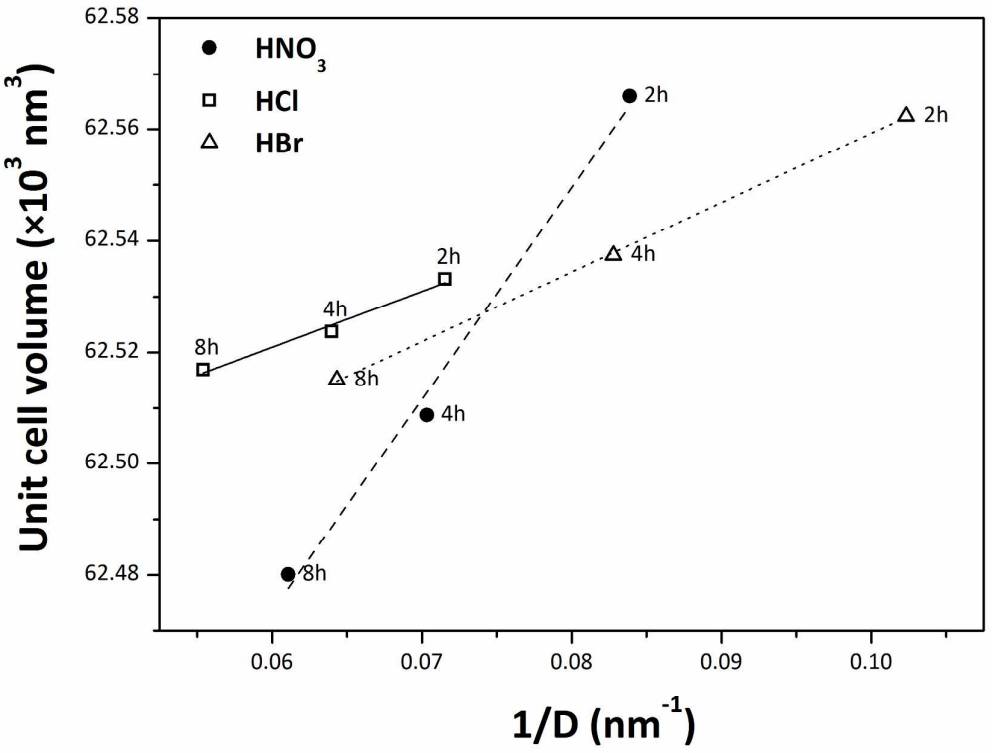

Fig. 9b

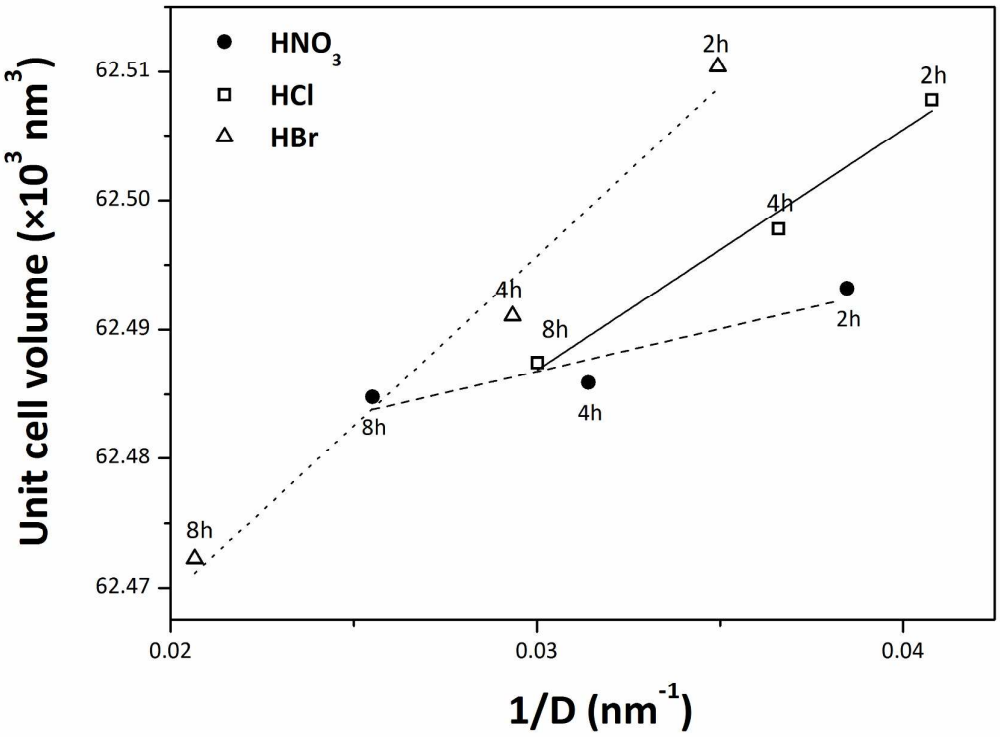

Fig. 9c

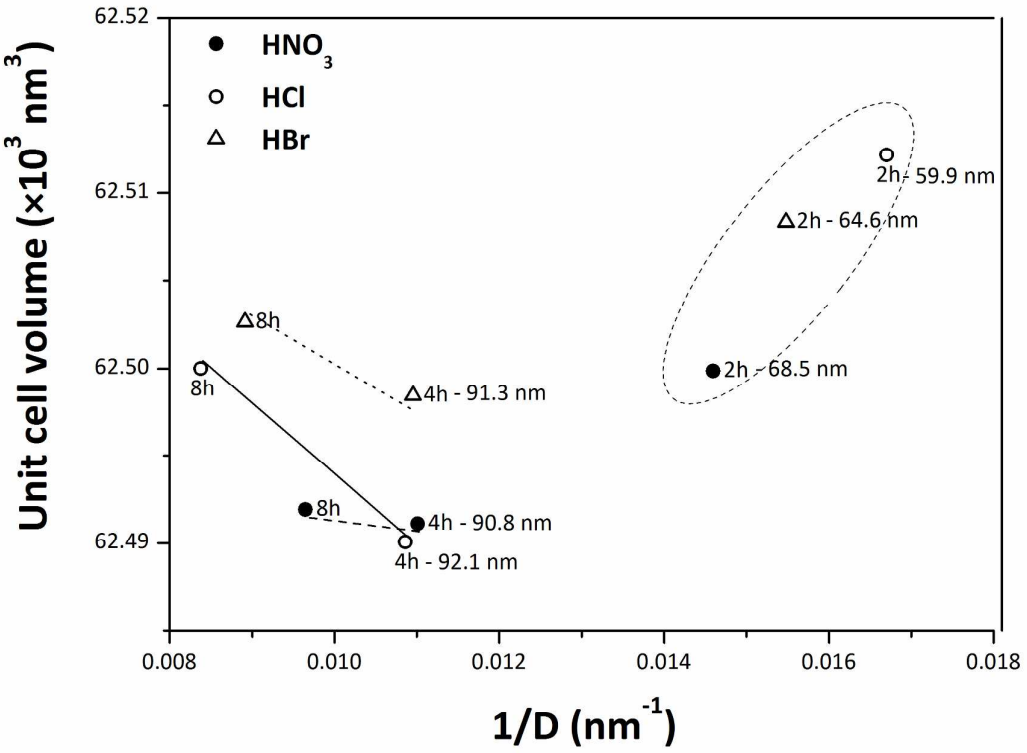

TABLES

Table 1 − Rietveld agreement factors and phase composition of samples with HNO_3 as source of counter-ions. The phase composition was calculated from the Rietveld refinements of X-ray diffraction patterns, using the NIST 676a internal standard.

Sample	No. of variables	Agreement factors				Phase composition			
		$R(_F^2)$ (%)	R_{wp} (%)	χ^2		anatase (wt%)	rutile (wt%)	brookite (wt%)	amorphous (wt%)
HNO_3 75	19	3.17	7.73	3.61		57.5±0.6	1.8±0.2	8.9±0.5	31.7±0.8
HNO_3 450 2h	19	3.35	5.26	1.83		49.4±0.4	14.8±0.2	18.5±0.3	17.3±0.5
HNO_3 450 4h	20	4.73	6.49	2.57		48.4±0.4	18.1±0.2	16.8±0.3	16.7±0.6
HNO_3 450 8h	20	4.59	6.71	2.64		48.9±0.4	21.1±0.2	15.4±0.4	14.6±0.6
HNO_3 600 2h	21	8.39	7.09	1.93		21.8±0.3	66.4±0.8	−	11.9±0.8
HNO_3 600 4h	21	7.99	8.67	3.80		12.9±0.2	78.1±0.8	−	9.0±0.8
HNO_3 600 8h	20	8.47	8.86	4.00		10.0±0.2	84.1±1.1	−	5.9±1.1
HNO_3 800 2h	14	11.57	10.13	4.74		−	92.6±1.2	−	7.4±1.2
HNO_3 800 4h	15	9.37	8.79	5.87		−	98.4±1.2	−	1.6±1.2†
HNO_3 800 8h	14	10.42	10.03	5.56		−	99.5±1.4	−	0.5±1.4†

† Values of amorphous phase less than 2 wt% are under the detection limit of the Rietveld−RIR method.

Table 2 – Rietveld agreement factors and phase composition of samples with HCl as source of counter-ions. The phase composition was calculated from the Rietveld refinements of X-ray diffraction patterns, using the NIST 676a internal standard.

Sample	No. of variables	Agreement factors				Phase composition			
		$R(_F^2)$ (%)	R_{wp} (%)	χ^2		anatase (wt%)	rutile (wt%)	brookite (wt%)	amorphous (wt%)
HCl 75	16	3.39	6.56	2.38		47.5±0.4	0.2±0.1	20.4±0.3	31.9±0.5
HCl 450 2h	21	4.28	5.60	2.24		35.7±0.4	25.5±0.3	22.8±0.3	16.0±0.6
HCl 450 4h	20	5.42	7.13	2.76		36.3±0.4	31.8±0.3	17.5±0.4	14.4±0.6
HCl 450 8h	21	5.55	6.57	2.52		39.8±0.3	32.7±0.3	14.5±0.3	13.0±0.5
HCl 600 2h	19	7.67	7.32	1.93		21.0±0.3	65.0±0.8	–	14.1±0.8
HCl 600 4h	21	9.39	8.79	3.90		29.7±0.3	63.2±0.6	–	7.1±0.7
HCl 600 8h	19	9.13	7.14	3.86		18.4±0.2	76.5±0.7	–	5.1±0.7
HCl 800 2h	14	9.32	10.42	3.44		–	94.8±2.8	–	5.2±2.8
HCl 800 4h	14	9.91	10.56	5.53		–	97.1±1.3	–	2.9±1.3
HCl 800 8h	13	10.72	11.91	6.76		–	98.9±1.4	–	1.1±1.4†

† Values of amorphous phase less than 2 wt% are under the detection limit of the Rietveld–RIR method.

Table 3 − Rietveld agreement factors and phase composition of samples with HBr as source of counter-ions. The phase composition was calculated from the Rietveld refinements of X-ray diffraction patterns, using the NIST 676a internal standard.

Sample	No. of variables	Agreement factors				Phase composition			
		$R(_F^2)$ (%)	R_{wp} (%)	χ^2		anatase (wt%)	rutile (wt%)	brookite (wt%)	amorphous (wt%)
HBr 75	22	4.30	4.27	1.82		51.5±0.4	3.5±0.1	13.2±0.3	31.8±0.5
HBr 450 2h	21	3.53	5.82	2.08		55.6±0.4	14.9±0.2	14.7±0.4	14.8±0.6
HBr 450 4h	20	3.83	6.05	2.31		55.1±0.4	15.7±0.2	15.8±0.4	13.3±0.6
HBr 450 8h	18	6.02	8.63	4.12		58.9±0.3	16.2±0.2	16.5±0.5	8.5±0.6
HBr 600 2h	19	9.87	7.44	3.04		27.5±0.4	61.8±0.8	−	10.7±0.9
HBr 600 4h	18	8.30	8.92	4.12		23.1±0.3	69.7±0.8	−	7.2±0.9
HBr 600 8h	18	8.32	9.19	4.38		9.0±0.2	86.5±1.0	−	4.5±1.0
HBr 800 2h	14	11.12	10.40	4.92		−	95.2±1.3	−	4.8±1.3
HBr 800 4h	14	10.47	10.99	5.99		−	96.7±1.3	−	3.3±1.3
HBr 800 8h	13	10.16	11.17	6.54		−	98.0±1.2	−	2.0±1.2†

† Values of amorphous phase less than 2 wt% are under the detection limit of the Rietveld−RIR method.

Table 4 – WPPM agreement factors, average crystalline domain diameters and mode of the size distribution of anatase (ant), rutile (rt), and brookite (brk) of samples with HNO_3 as source of counter-ions.

	Agreement factors			Average crystalline domain diameter (nm)			Mode of the size distribution (nm)		
Sample	R_{wp} (%)	R_{exp} (%)	χ^2	$\langle D_{ant} \rangle$	$\langle D_{rt} \rangle$	$\langle D_{brk} \rangle$	Ant	Rt	Brk
HNO_3 75	2.63	1.90	1.38	3.3±0.1	4.7±0.1	2.7±0.3	3.1±0.1	3.1±0.1	1.7±0.2
HNO_3 450 2h	5.87	1.96	3.00	9.7±0.1	11.9±0.1	5.0±0.1	8.5±0.1	7.5±0.1	3.3±0.1
HNO_3 450 4h	5.60	2.11	2.65	10.3±0.1	14.2±0.1	6.7±0.1	8.8±0.1	9.4±0.1	6.1±0.1
HNO_3 450 8h	7.18	2.03	3.54	12.2±0.1	16.4±0.1	7.0±0.1	10.0±0.1	11.7±0.1	6.7±0.1
HNO_3 600 2h	3.97	2.05	1.94	24.3±0.1	26.0±0.1	–	19.0±0.1	18.0±0.1	–
HNO_3 600 4h	4.14	2.15	1.93	27.3±1.3	31.8±0.5	–	21.0±1.0	22.3±0.4	–
HNO_3 600 8h	4.05	2.14	1.89	28.6±0.1	39.2±0.1	–	22.7±0.1	30.4±0.1	–
HNO_3 800 2h	7.53	2.13	3.54	–	68.5±1.3	–	–	60.6±1.2	–
HNO_3 800 4h	7.86	2.25	3.50	–	90.8±2.3	–	–	90.4±2.3	–
HNO_3 800 8h	7.82	2.21	3.54	–	103.7±2.7	–	–	103.3±2.7	–

Table 5 – WPPM agreement factors, average crystalline domain diameters and mode of the size distribution of anatase (ant), rutile (rt), and brookite (brk) of samples with HCl as source of counter-ions.

	Agreement factors			Average crystalline domain diameter (nm)			Mode of the size distribution (nm)		
Sample	R_{wp} (%)	R_{exp} (%)	χ^2	$\langle D_{ant} \rangle$ (nm)	$\langle D_{rt} \rangle$ (nm)	$\langle D_{brk} \rangle$ (nm)	Ant	Rt	Brk
HCl 75	2.98	1.92	1.56	3.2±0.1	4.9±0.1	3.8±0.4	3.0±0.1	3.5±0.1	2.8±0.3
HCl 450 2h	7.88	2.02	3.91	9.0±0.1	14.0±0.1	7.9±0.1	6.3±0.1	9.3±0.1	7.3±0.1
HCl 450 4h	6.82	2.03	3.35	9.7±0.1	15.6±0.1	8.8±0.1	7.6±0.1	10.0±0.1	8.0±0.1
HCl 450 8h	4.75	2.02	2.35	10.4±0.1	18.0±0.1	10.6±0.1	7.8±0.1	12.7±0.1	9.9±0.1
HCl 600 2h	7.49	2.07	3.62	20.9±0.1	24.5±0.1	–	16.1±0.1	18.3±0.1	–
HCl 600 4h	4.13	2.10	1.96	24.2±0.5	27.3±0.4	–	18.1±0.4	19.6±0.3	–
HCl 600 8h	4.16	2.10	1.98	31.3±0.1	33.3±0.1	–	26.6±0.1	25.2±0.1	–
HCl 800 2h	7.76	2.07	3.75	–	59.9±1.0	–	–	51.9±0.9	–
HCl 800 4h	7.72	2.23	3.46	–	92.1±9.9	–	–	91.7±9.8	–
HCl 800 8h	8.38	2.26	3.71	–	119.3±4.0	–	–	118.8±4.0	–

Table 6 – WPPM agreement factors, average crystalline domain diameters and mode of the size distribution of anatase (ant), rutile (rt), and brookite (brk) of samples with HBr as source of counter-ions.

	Agreement factors			Average crystalline domain diameter (nm)			Mode of the size distribution (nm)		
Sample	R_{wp} (%)	R_{exp} (%)	χ^2	$\langle D_{ant} \rangle$ (nm)	$\langle D_{rt} \rangle$ (nm)	$\langle D_{brk} \rangle$ (nm)	Ant	Rt	Brk
HBr 75	2.00	1.40	1.42	3.5±0.1	4.5±0.1	3.9±0.1	3.4±0.1	3.9±0.1	3.2±0.1
HBr 450 2h	6.19	1.95	3.18	6.1±0.1	9.8±0.1	6.8±0.1	3.4±0.1	6.4±0.1	5.4±0.1
HBr 450 4h	4.64	2.02	2.30	7.8±0.2	12.1±0.5	7.6±0.6	5.6±0.2	8.3±0.3	6.6±0.6
HBr 450 8h	6.34	1.98	3.20	8.8±0.1	15.5±0.1	9.2±0.1	5.9±0.1	11.8±0.1	8.7±0.1
HBr 600 2h	4.87	2.08	2.34	25.8±0.1	28.6±0.1	–	20.3±0.1	21.0±0.1	–
HBr 600 4h	4.22	2.15	1.96	28.5±0.1	34.1±0.1	–	22.0±0.1	24.4±0.1	–
HBr 600 8h	4.51	2.14	2.10	36.7±0.1	48.4±0.1	–	32.4±0.1	40.1.2±0.1	–
HBr 800 2h	7.58	2.07	3.66	–	64.6±1.3	–	–	54.0±1.1	–
HBr 800 4h	7.90	2.21	3.57	–	91.3±2.1	–	–	89.7±2.1	–
HBr 800 8h	8.26	2.21	3.74	–	112.2±3.2	–	–	108.9±3.1	–

Table 7 – Unit cell parameters of anatase, rutile and brookite in the samples, as calculated *via* the WPPM modelling of samples with HNO_3 as source of counter-ions.

	Unit cell parameters									
	Anatase			Rutile			Brookite			
Sample	*a* = *b* (nm)	*c* (nm)	Volume (nm^3)	*a* = *b* (nm)	*c* (nm)	Volume (nm^3)	*a* (nm)	*b* (nm)	*c* (nm)	Volume (nm^3)
HNO_3 75	0.3799(6)	0.9513(107)	0.137(2)	0.4621(6)	0.2954(7)	0.063(1)	0.5551(26)	0.9184(25)	0.5171(14)	0.264(3)
HNO_3 450 2h	0.3791(1)	0.9515(1)	0.137(1)	0.4598(1)	0.2959(1)	0.063(1)	0.5440(2)	0.9206(4)	0.5157(1)	0.258(1)
HNO_3 450 4h	0.3786(1)	0.9515(2)	0.136(1)	0.4596(1)	0.2959(1)	0.063(1)	0.5277(3)	0.9101(5)	0.5386(6)	0.259(1)
HNO_3 450 8h	0.3786(1)	0.9514(1)	0.136(1)	0.4595(1)	0.2959(1)	0.062(1)	0.5327(5)	0.9080(7)	0.5400(10)	0.261(1)
HNO_3 600 2h	0.3785(1)	0.9523(1)	0.136(1)	0.4594(1)	0.2961(1)	0.062(1)				–
HNO_3 600 4h	0.3784(1)	0.9521(1)	0.136(1)	0.4594(1)	0.2960(1)	0.062(1)				–
HNO_3 600 8h	0.3784(1)	0.9522(1)	0.136(1)	0.4594(1)	0.2960(1)	0.062(1)				–
HNO_3 800 2h			–	0.4594(1)	0.2961(1)	0.062(1)				–
HNO_3 800 4h			–	0.4594(1)	0.2960(1)	0.062(1)				–
HNO_3 800 8h			–	0.4594(1)	0.2961(1)	0.062(1)				–

Table 8 − Unit cell parameters of anatase, rutile and brookite in the samples, as calculated *via* the WPPM modelling of samples with HCl as source of counter-ions.

	Unit cell parameters									
	Anatase			Rutile			Brookite			
Sample	*a* = *b* (nm)	*c* (nm)	Volume (nm^3)	*a* = *b* (nm)	*c* (nm)	Volume (nm^3)	*a* (nm)	*b* (nm)	*c* (nm)	Volume (nm^3)
HCl 75	0.3788(2)	0.9470(23)	0.135(1)	0.4564(7)	0.2940(13)	0.061(1)	0.5463(19)	0.9130(48)	0.5174(11)	0.258(3)
HCl 450 2h	0.3788(1)	0.9513(1)	0.137(1)	0.4597(1)	0.2960(1)	0.063(1)	0.5439(2)	0.9191(5)	0.5152(2)	0.258(1)
HCl 450 4h	0.3786(1)	0.9495(1)	0.136(1)	0.4596(1)	0.2960(1)	0.063(1)	0.5503(6)	0.9199(11)	0.5154(3)	0.261(1)
HCl 450 8h	0.3786(1)	0.9511(1)	0.136(1)	0.4597(1)	0.2959(1)	0.063(1)	0.5447(1)	0.9156(6)	0.5169(3)	0.258(1)
HCl 600 2h	0.3786(1)	0.9518(1)	0.136(1)	0.4595(1)	0.2960(1)	0.063(1)				–
HCl 600 4h	0.3786(1)	0.9518(1)	0.136(1)	0.4595(1)	0.2960(1)	0.062(1)				–
HCl 600 8h	0.3785(1)	0.9518(1)	0.136(1)	0.4595(1)	0.2960(1)	0.062(1)				–
HCl 800 2h			–	0.4595(1)	0.2961(1)	0.063(1)				–
HCl 800 4h			–	0.4594(1)	0.2961(1)	0.062(1)				–
HCl 800 8h			–	0.4595(1)	0.2961(1)	0.063(1)				–

Table 9 − Unit cell parameters of anatase, rutile and brookite in the samples, as calculated *via* the WPPM modelling of samples with HBr as source of counter-ions.

	Unit cell parameters									
	Anatase			Rutile			Brookite			
Sample	*a* = *b* (nm)	*c* (nm)	Volume (nm^3)	*a* = *b* (nm)	*c* (nm)	Volume (nm^3)	*a* (nm)	*b* (nm)	*c* (nm)	Volume (nm^3)
HBr 75	0.3829(10)	0.9726(110)	0.143(2)	0.4614(29)	0.2957(68)	0.063(2)	0.5414(39)	0.9302(140)	0.5122(51)	0.258(6)
HBr 450 2h	0.3788(1)	0.9512(1)	0.137(1)	0.4598(1)	0.2959(1)	0.063(1)	0.5478(1)	0.9159(3)	0.5146(2)	0.258(1)
HBr 450 4h	0.3788(1)	0.9513(1)	0.136(1)	0.4597(1)	0.2959(1)	0.063(1)	0.5527(3)	0.9127(7)	0.5145(3)	0.260(1)
HBr 450 8h	0.3787(1)	0.9516(1)	0.136(1)	0.4596(1)	0.2959(1)	0.063(1)	0.5571(2)	0.9114(3)	0.5157(2)	0.262(1)
HBr 600 2h	0.3785(1)	0.9523(1)	0.136(1)	0.4595(1)	0.2961(1)	0.063(1)				–
HBr 600 4h	0.3785(1)	0.9523(1)	0.136(1)	0.4595(1)	0.2960(1)	0.062(1)				–
HBr 600 8h	0.3784(1)	0.9523(1)	0.136(1)	0.4594(1)	0.2960(1)	0.062(1)				–
HBr 800 2h			–	0.4595(1)	0.2961(1)	0.063(1)				–
HBr 800 4h			–	0.4595(1)	0.2961(1)	0.062(1)				–
HBr 800 8h			–	0.4595(1)	0.2961(1)	0.063(1)				–

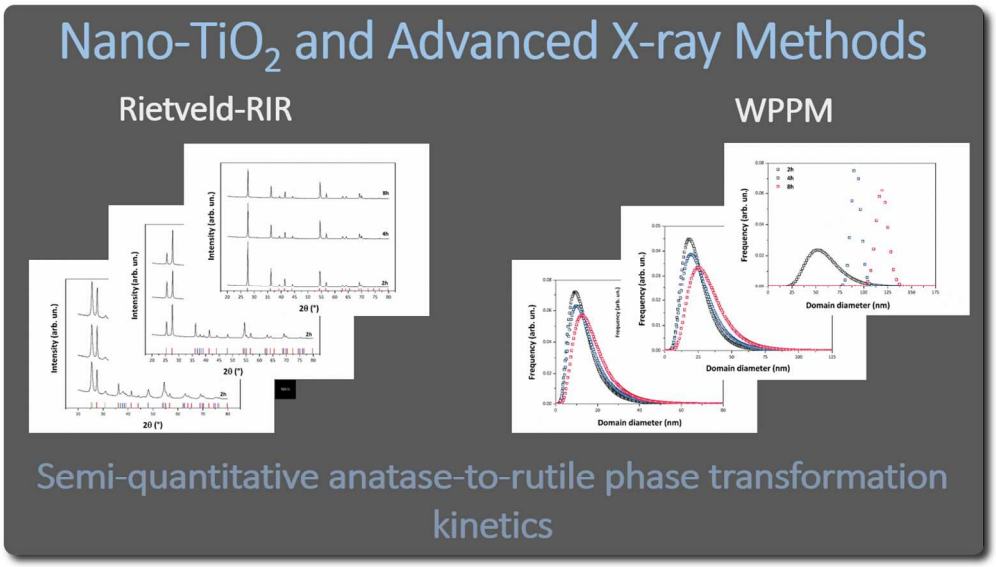

492x281mm (72 x 72 DPI)